T.C.
TÜRKİYE ENERJİ, NÜKLEER VE MADEN ARAŞTIRMA KURUMU
Akademi ve Yayınlar Koordinatörlüğü

Sayı : E-97996550-824.02.99-90685

Konu : TENMAK Akademik Dergisi

YÜKSEKÖĞRETİM KURULU BAŞKANLIĞINA

Türkiye Enerji, Nükleer ve Maden Araştırma Kurumu (TENMAK) tarafından yayımlanmakta olan *Turkish Journal of Nuclear Sciences* dergisinde nükleer, radyasyon ve hızlandırıcı teknolojilerine yönelik bilimsel çalışmalara yer verilmektedir. Belirtilen alanlarda bilimsel çalışmalar yürüten üniversitelerin özgün nitelikteki makalelerinin yayınlanmasına açık olan dergimizin, yakın zamanda uluslararası bilimsel indekslerde yer alması hedeflenmektedir. Bu kapsamda ekte sunulan dergi tanıtım metninin ve derginin yayımlanmış son sayısının Başkanlığınız altında bulunan üniversitelerin Fen ve Mühendislik Fakülteleri ile Fen Bilimleri ve Nükleer Bilimler Enstitülerine iletilmesi faydalı olacaktır.

Gereğini arz ederim

Prof. Dr. Abdulkadir BALIKÇI
Başkan

Ek:

1 - Dergi Tanıtım Metni (1 Sayfa)

2 - TJNS Yayınlanmış Son Sayı (33 Sayfa)

TENMAK- Akademi ve Yayınlar Koordinatörlüğü, Emniyet Mah. Ankara Üniversitesi Beşevler 10. Yıl Yerleşkesi, 06100, Yenimahalle/ANKARA
Tel : 3122126230
Fax : 3122226421
KEP Adresi : tenmak@hs01.kep.tr

Bilgi için:Serdar BULUT
Fizikçi

TENMAK
TURKISH ENERGY, NUCLEAR AND MINERAL RESEARCH AGENCY

TURKISH JOURNAL OF NUCLEAR SCIENCES
Journal homepage https://dergipark.org.tr/en/pub/tjns

Değerli Bilim İnsanları,

Türkiye Enerji, Nükleer ve Maden Araştırma Kurumu (TENMAK) tarafından yayımlanmakta olan Turkish Journal of Nuclear Sciences dergisinde nükleer, radyasyon ve hızlandırıcı teknolojilerine yönelik bilimsel çalışmalara yer verilmektedir.

1974 yılında basılı olarak "Technical Journal" adıyla yayımlanmaya başlayan ve daha sonrasında "Turkish Journal of Nuclear Sciences" adıyla 2003 yılına kadar yayımlanmış olan olan dergi, aynı isimle 2018 yılından itibaren sadece elektronik olarak, İngilizce yayın dilinde, Haziran ve Aralık aylarında olmak üzere yılda iki kez yayımlanmaya devam etmektedir.

Dergimiz, Dergipark Akademik ev sahipliğinde ULAKBİM Temel Bilimler Veri Tabanında açık erişimli taranan bilimsel ve ulusal/uluslararası hakemli bir dergidir.

Turkish Journal of Nuclear Sciences Dergisi'ne elektronik ortamda **(https://dergipark.org.tr/tr/pub/tjns)** makale başvurusu yapılabilmekte ve yayımlanan makalelere ulaşılabilmektedir.

Nükleer ve hızlandırıcı teknolojisi ile radyasyon uygulamaları alanında çalışmalar yürütün bilim insanlarının özgün nitelikteki makalelerinin yayınlanmasına açık olan dergimizin bilimsel indekslerde yer alması hedeflenmektedir.

Dergimize makale göndererek vereceğiniz katkı ve destekleriniz için şimdiden teşekkür ederiz.

Prof. Dr. Abdülkadir BALIKÇI
TENMAK Başkanı

TURKISH ENERGY, NUCLEAR AND MINERAL RESEARCH AGENCY
TURKISH JOURNAL OF NUCLEAR SCIENCES
Journal Web Address: https://dergipark.org.tr/en/pub/tjns

TENMAK
TURKISH ENERGY, NUCLEAR AND MINERAL RESEARCH AGENCY
Mustafa Kemal Mahallesi, Dumlupınar Blv. No:192, 06510 Çankaya/Ankara
Phone:+90 312 295 8700 (Santral) - 444 8235
Fax:+90 312 295 87 61 E-mail:journal@tenmak.gov.tr

Volume: 34-35 No:1 2022
e-ISSN-2791-7185
Dergi elektronik olup, örnektir

TURKISH JOURNAL OF NUCLEAR SCIENCES

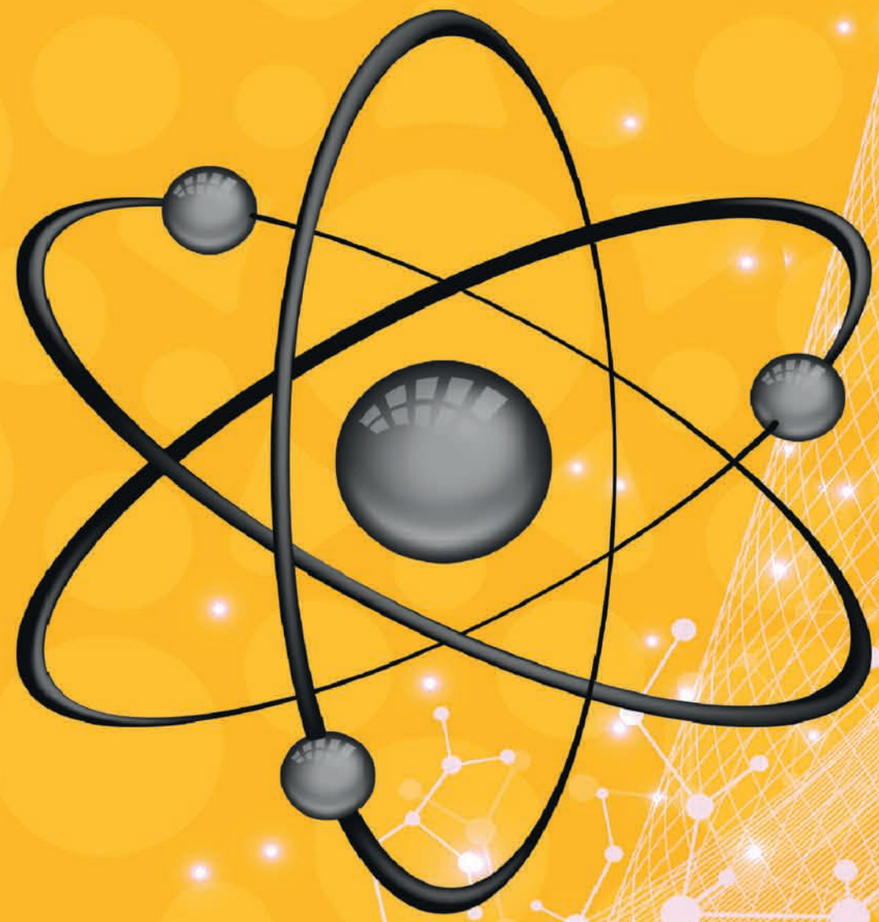

Volume: 34-35 No:1 2022

e-ISSN-2791-7185
Dergi elektronik olup, örnektir

TURKISH JOURNAL OF NUCLEAR SCIENCES

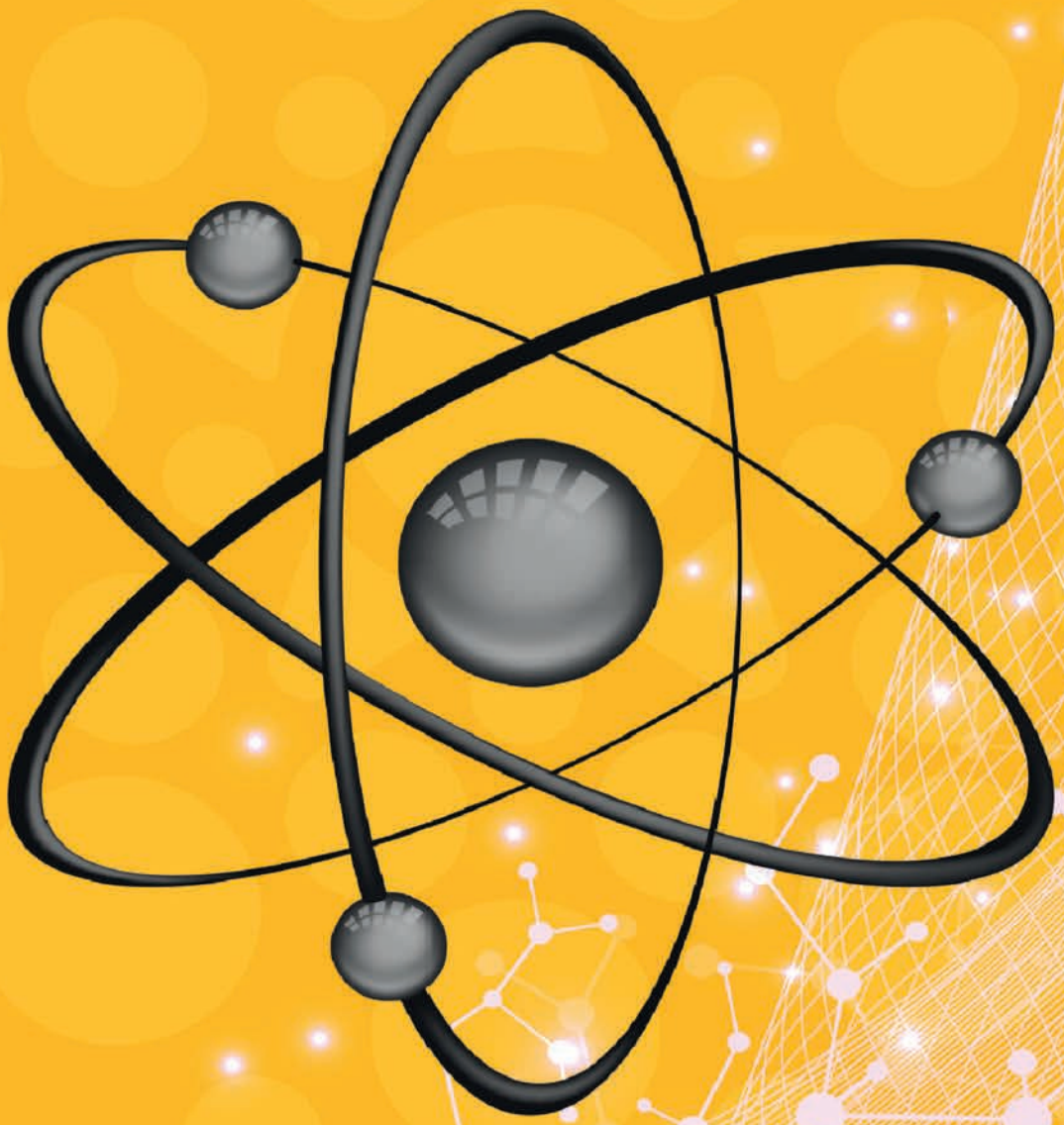

Volume:34-35 No:1 2022 ISSN-2791-7185

TURKISH ENERGY, NUCLEAR AND MINERAL RESEARCH AGENCY
Turkish Journal of Nuclear Sciences

Türkiye Enerji, Nükleer ve Maden Araştırma Kurumu (TENMAK) Matbaası
Mustafa Kemal Mahallesi, Dumlupınar Blv. No:192, 06510 Çankaya/Ankara
Tel:+90 312 295 8700 (Santral) - 444 8235 Faks: +90 312 295 87 61
Basım Tarihi: Ocak 2023

ISSN-2791-7185

Journal Identity

Journal Title	**:** Turkish Journal of Nuclear Sciences
Electronic ISSN	**:** ISSN-2791-7185
Language	**:** English
Web address	: https://dergipark.org.tr/en/pub/tjns
E-Mail official adress	: journal@tenmak.gov.tr
Publishing Type	: Periodically
Publishing Interval	: Every six months (Twice a year)
Founding Year	: 1981
Publisher	: Turkish Energy, Nuclear and Mineral Research Agency
Publishing Adress	**:**Turkish Energy, Nuclear and Mineral Research Agency (TENMAK), Mustafa Kemal Mahallesi, Dumlupınar Blv. No:192, 06510 Çankaya/Ankara

Contact

TENMAK Academy and Publications Department,

Ankara Üniversitesi 10. Yıl Tandoğan Yerleşkesi, 06100, Beşevler/ANKARA

Phone:+90 312 212 62 30 Fax: +90 312 222 64 21

Web adress: https://dergipark.org.tr/en/pub/tjns

Turkish Journal of Nuclear Sciences
Volume: 34-35 No:1 2022

Dear Scientists,

Turkish Journal of Nuclear Sciences, published by TENMAK, publishes scientific studies on nuclear and radiation Technologies

Our journal started to be published in printed form in 1974 under the name of "Technical Journal", then it was named "Turkish Journal of Nuclear Sciences" and continued its publication until 2003.

Interrupted its publication for a while, our journal has been published twice a year, in June and December, only electronically since 2018.

Our journal is national and international refereed and aims to include original articles in scientific indexes.

We would like to thank the authors who enrich our journal with their publications and the valuable scientists in the editorial and referee boards who contribute to the journal with their evaluations. Best regards.

Prof. Dr. Abdulkadir BALIKÇI

Aims Scope

Turkish Journal of Nuclear Sciences is published to meet the needs of the public and researchers in this field by publishing scientific studies conducted in Türkiye to ensure the use of atomic energy for the benefit of the country.

The Turkish Journal of Nuclear Sciences includes scientific articles on nuclear and radiation technologies.

Turkish Journal of Nuclear Sciences
Volume: 34-35 No:1 2022

CONTENTS

Research Articles

TENMAK TURKISH ENERGY, NUCLEAR AND MINERAL RESEARCH AGENCY

TURKISH JOURNAL OF NUCLEAR SCIENCES

Journal homepage https://dergipark.org.tr/en/pub/tjns

MEASUREMENT OF S-FACTOR FOR THE ^{11}B(p, α)2α REACTION AT LOW ENERGIES: CARBON BUILD-UP EFFECT

Osman ALAÇAYIR[1)], Nilgün BAYDOĞAN[2)], Tamer YALÇIN[1)], Adnan BAYKAL[1)], Recep BIYIK[1*)]

1) Turkish Energy, Nuclear and Mineral Research Agency, Nuclear Energy Research Institute, Küçükçekmece, 34303 İstanbul/TÜRKİYE

2) Istanbul Technical University, Energy Institute, Maslak, 34469 İstanbul/TÜRKİYE

*recep.biyik@tenmak.gov.tr

DÜŞÜK ENERJİLERDE ^{11}B(p, α)2α REAKSİYONU İÇİN S-FAKTÖRÜNÜN ÖLÇÜMÜ: KARBON BUILD-UP ETKİSİ

Abstract:

The astrophysical S-factor for the ^{11}B(p, α)2α reaction has been evaluated at effective center of mass (CM) energies of 110, 113, 115, 117, 119, 121, 124, 126, 128, 131, and 133 keV. It was observed that there was a significant difference between the calculated values and the literature values. Another difference with literature is the increased yield ratio N_0/N_1 of the reaction channels $^{11}B(p,\alpha_0)^8Be$ and $^{11}B(p,\alpha_1)^8Be$ with increasing energy. The reason for the discrepancy was attributed to being carbon build-up on the target surface during irradiation. Due to the Carbon build-up effect in the energy range studied, effective energy (E_{eff}) values for the ^{11}B(p, α)2α reaction decreased by about 30 keV.

Özet:

^{11}B(p, α)2α reaksiyonu için astrofiziksel S faktörü, 110, 113, 115, 117, 119, 121, 124, 126, 128, 131 ve 133 keV etkin kütle merkezi (CM) enerjilerinde değerlendirilmiştir. Hesaplanan değerler ile literatür değerleri arasında anlamlı bir farklılık olduğu görülmüştür. Literatürle olan diğer bir fark, artan enerji ile $^{11}B(p,\alpha_0)^8Be$ ve $^{11}B(p,\alpha_1)^8Be$ reaksiyon kanallarının N_0/N_1 verim oranının artmasıdır. Elde edilen değerlerin literatür değerleri ile farklılaşmasının nedeni, ışınlama sırasında hedef yüzeyde uluşan karbon birikmesine atfedildi. İncelenen enerji aralığındaki karbon birikimi etkisi nedeniyle, ^{11}B(p, α)2α reaksiyonu için etkin enerji (E_{eff}) değerleri yaklaşık olarak 30 keV azaldığı görüldü.

Keywords: S-factor, carbon build-up, ^{11}B(p, α)^{8}Be, ^{11}B(p, α)2α reaction,

Anahtar Kelimeler: S-faktörü, Karbon build-up, ^{11}B(p, α)^{8}Be, ^{11}B(p, α)2α reaksiyonu,

1. Introduction

The $^{11}B(p,\alpha)^8Be$ reaction has been the focus of researchers since the 1930s and was first studied by Oliphant and Rutherford (Oliphant & Rutherford, 1933). Interest in the reaction tends to increase in recent years, with the increasing number of studies on aneutronic fusion (Belyaev et al., 2015, Wessel et al., 2000). Contrary to conventional fusion reactors where D-T reaction is used, $^{11}B(p,\alpha)^8Be$ appears to be more advantageous in terms of radioactive contamination since there are no neutrons generated in the reactors utilizing this reaction. Another reason for the interest in the reaction is the need to know the reaction rates of this reaction in order to understand the relative abundances of B, Li, and Be in astrophysical studies (Boesgaard et al., 2005, Lamia et al., 2011).

Techniques such as nuclear reaction analysis (NRA), Rutherford backscattering spectrometry (RBS), heavy ion recoil detection analysis (HERDA) are used to determine the distribution of elements on various material surfaces. NRA is used in conjunction with the RBS as a complementary method. Its sensitivity in light elements is the advantage of NRA over RBS. Depth analysis of light elements can be performed at the nanometer (nm) level thanks to NRA. NRA using the $^{11}B(p,\alpha_0)^8Be$ reaction has two important advantages; having a high cross-section and an alpha peak that is completely isolated from the energy of protons impinged on the surface, thus minimizing the margin of error arising from data analysis (Kokkoris et al., 2010), (Mayer et al., 1998). Furthermore, the experimental method used in NRA and RBS is almost the same with the method used in the present study. This increases the importance of the present study to gain infrastructure for some ion beam applications (IBA) like NRA and RBS.

The $^{11}B(p,3\alpha)$ reaction basically has the possibility to occur through three different channels;

Channel.1 $p+{}^{11}B\rightarrow{}^{12}C^*\rightarrow {}^8Be+\alpha_0\rightarrow \alpha_{01}+\alpha_{02}+\alpha_0$

Channel.2 $p+{}^{11}B\rightarrow{}^{12}C^*\rightarrow {}^8Be^*+\alpha_1\rightarrow\alpha_{11}+\alpha_{12}+\alpha_1$

Channel.3 $p+{}^{11}B\rightarrow{}^{12}C^*\rightarrow \alpha_{21}+\alpha_{22}+\alpha_{23}$

Channels 1 and 2 are called sequential reactions, while channel 3 is called direct reactions. No evidence was found in the analyses that the reaction took place through the 3rd channel. All findings point to sequential decay. While the decays occur in the 1st channel to the ground state energy level of the ^{8}Be nucleus, the reactions from the 2nd channel take place to the 1st excited level of the ^{8}Be nucleus (Becker et al., 1987).

In this study, S-Factor of the $^{11}B(p,\alpha_0)^8Be$ and $^{11}B(p,\alpha_1)^8Be^*$ reaction channels at effective energy range 110-133 keV (CM) and at 135º detector angle was measured. The energies are effective CM energies calculated by considering the stopping power of the thick target (56μg/cm^2) used in the experiment. Yield ratios of the first and second reaction channels are calculated for the energies studied. When the S-factor values, obtained in this study, were compared with the literature values, there is a significant difference. It was considered that the carbon build-up effect was the reason for the difference and according to the results, this effect causes approximately 30 keV to decrease E_{eff} values at the energy range studied.

Carbon build-up is the accumulation of some organic compounds on surfaces irradiated with ions in ion beam applications. This effect mainly occurs because of some hydrocarbons and other gases like CO, CO_2, H_2O etc. remained in the vacuum chamber. These gases are usually vapors of vacuum pump oils or vacuum greases and gases released from o-rings, the walls of the vacuum chamber etc.. The other most important reason for carbon build-up is the various organic residues accumulated on the target material that is not cleaned sufficiently before irradiation.

*Corresponding author: Recep BIYIK, Turkish Energy, Nuclear and Mineral Research Agency, Nuclear Energy Research Institute, Küçükçekmece, 34303 İstanbul/TÜRKİYE, E-mail:recep.biyik@tenmak.gov.tr ORCID:0000-0001-7929-4395 Gönderim: 21/02/2022 Kabul: 28/06/2022.

2. Experimental

Irradiations were carried out in the SAMES J-15 ion accelerator installed in Nuclear Energy Research Institute (NUKEN), Istanbul. SAMES J-15 accelerator is a Van de Graff type accelerator with a maximum voltage of 150 kV (Fig. 1). The ion source is an RF type with an extraction voltage of 5kV. A detailed explanation about J-15 Accelerator can be found at the (Alaçayır, 2015, Baykal, 1997, Tarcan et al., 1998).

The scattering chamber (Alaçayır, 2015, Baykal, 1997) experimental set-up, and counting system are shown in Figure 2. The scattering chamber is a cylindrical vacuum chamber made of stainless steel with a diameter of approximately 250 mm and a depth of 85 mm. The target holder placed in the centre can be moved vertically thanks to a rotary-linear feedthrough without disturbing the vacuum, so that different points of the target can be irradiated. The target holder can be rotated around its own axis so that the beam angle can be adjusted. Two surface-barrier detectors can be placed inside the vacuum chamber, one of which is fixed and the other can be rotated 360° around the target with the help of a rotary feedthrough.

Figure 1. Low Energy Ion Accelerator- Sames J-15 and Van-de Graaff Generator

The collimators consist of three consecutive metal bracelets with an inner diameter of 3 mm. The current read in the micrometer, which gives the collimator current since they are in contact with each other, is the total current value of the three collimators. There is an electron suppresser ring in front of the target with an inner diameter of 10 mm (Fig. 2, *a*). The suppresser ring has a voltage of -180V while irradiations. A Beaudouin oil backing pump and an Edwards B04 model oil diffusion pump were used to maintain the vacuum in the beamline and scattering chamber at 5.0x 10^{-6} Torr during irradiation. Detection of alpha particles formed in the reaction was carried out with a 300 mm^2 surface barrier detector (Ametec-Ortec U-016-300-100, Ultra Ion-Implanted Detector) (Fig. 2, *b*). In the counting system, an Ortec 401B Bin, an Ortec 428 detector bias supply, a Canberra 2003B model preamplifier, a Canberra 2020 model amplifier, and a Canberra Multiport-II multichannel analyzer (MCA) were used (Fig. 2, *b*).

Irradiations were carried out at 5μA beam current for 4250 s. Beam current is measured during the irradiation with an Ortec 439 digital current integrator and an Ortec 875 Counter. On the other hand, because the beam energy was not sufficient, energy calibration could not be done for the accelerator. Hence the projectile/proton energy is taken directly as the high voltage value plus extraction voltage. The high voltage was measured with an error less than 1.0 keV.

After each irradiation, the target was shifted, and it has been ensured that all irradiations are carried out with a fresh target. The targets to be irradiated were prepared by thermal evaporation of natural B_2O_3 on thin aluminium foil at a pressure environment of 10^{-4} Torr. The target thickness was calculated as 56 μg/cm^2 as a result of the measurements made before and after coating.

Irradiations were carried out at 5μA beam current for 4250 s. Beam current is measured during the irradiation with an Ortec 439 digital current integrator and an Ortec 875 Counter. On the other hand, because the beam energy was not sufficient, energy calibration could not be done for the accelerator. Hence the projectile/proton energy is taken directly as the high voltage value plus extraction voltage. The high voltage was measured with an error less than 1.0 keV.

After each irradiation, the target was shifted, and it has been ensured that all irradiations are carried out with a fresh target. The targets to be irradiated were prepared by thermal evaporation of natural B_2O_3 on thin aluminium foil at a pressure environment of 10^{-4} Torr. The target thickness was calculated as 56 μg/cm^2 as a result of the measurements made before and after coating.

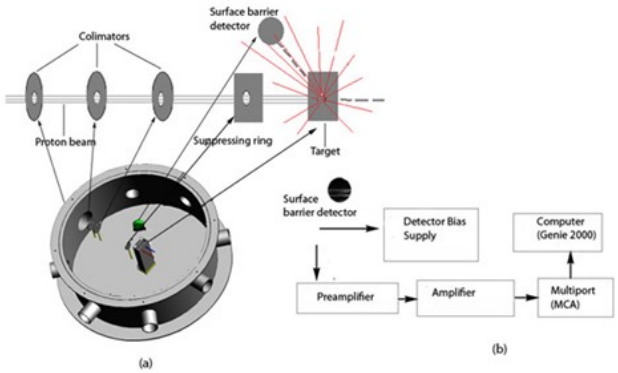

Figure 2. a) Experimental set up, scattered chamber (collimators, electron suppresser, target, and surface barrier detector) b) and counting system

Calibration of the surface-barrier detector was performed with an Amersham calibration source, consisting of Americium-241, Curium-244, Plutonium-239 isotopes (Amersham, 1992). Since the alpha counts caused by the vacuum environment are close to zero and the alpha counts caused by the reaction are only a few per second, the detector efficiency is accepted as 100%. The detector is placed at an angle of 135° with the direction of the beam. In order to prevent the photons scattered from the target from reaching the detector, a thin 250 μg/cm^2 aluminized mylar foil was used.

The solid angle is calculated assuming the target is closer to the elliptic geometry. Sacalc-Ellipsoid computer software (Whitcher, 2014) using the Monte Carlo method was used. Cross-section data calculated using the solid angle value resulting from the elliptic target approach were compared with the values in the literature.

3. Results and discussion

The alpha (α) particles emitted from the $^{11}B(p,\alpha)2\alpha$ reaction as a result of irradiation of the B_2O_3 target with protons at energies of 110-133 keV were counted with a surface-barrier detector. The alpha spectrum with different energies has been visualized with the Genie 2000 program. Alpha particle spectra have been obtained at effective CM energies 110, 113, 115, 117, 119, 121, 124, 126, 128, 131, 133 keV. As an example, the alpha spectrum for proton beam energy at 115 keV was given in Fig. 3. Although the counts at 115 keV proton energies is greater than the counts at the other energies it doesn't mean anything if the size of the error bars are considered (Fig.5). In the literature, although the cross section values are increased regularly in direct proportion to projectile/proton energy,

it seems our values are irregular.

The reason for this situation can be shown as the low homogeneity of the target thickness and the different Carbon build-up thickness for each irradiation. Since the α_0 peak is completely separate from the spectrum, the number of α_0 particles (N_0) was calculated directly using this peak. On the other hand, the α_1 peak is unfortunately intertwined with the secondary alpha counts. Since three particles are created after the reaction, one of which is the primary alpha particle (α_1) and the other two is secondary alpha particles (α_{11} and α_{12}), the total number of α_1 particles (N_1) was calculated by taking 1/3 of the total count in the spectrum (Stave et al., 2011, Davidson et al., 1979). As seen in the spectra, the low-energy region of the spectrum was cut to avoid electronic noise. The counts in this region were calculated by the extrapolation method (Fig. 4).

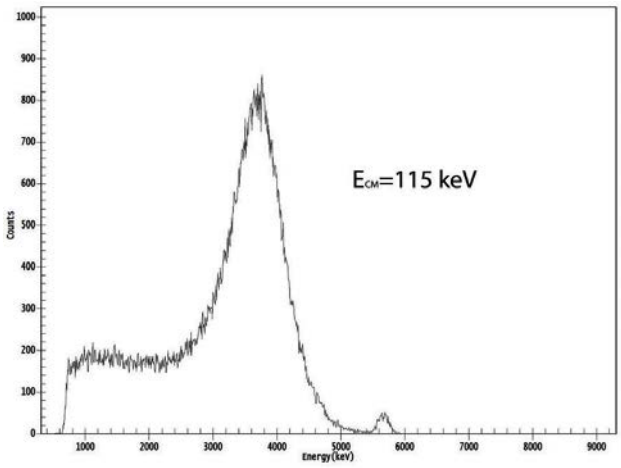

Figure 3. The alpha spectrum at ECM 115 keV of ^{11}B(p,α)2α reaction, the low energy region of the spectrum was cut to avoid the electronic noise.

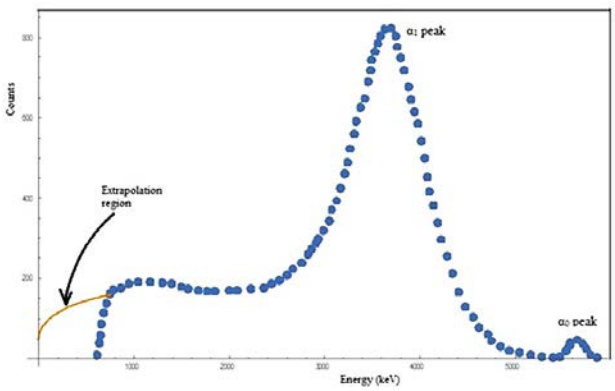

Figure 4. Alpha energy spectrum and extrapolation region

To determine the uncertainty in target thickness, different points of the target were bombarded with 117 keV (CM) energy protons. The α_0 yield was determined directly by taking the total counts under the α_0 peak in the obtained alpha spectra. The total uncertainty was calculated by taking the square root of the sum of the squares of the uncertainty that comes from the direct measuring of the target thickness and the uncertainty obtained from these counts.

The Stopping Range of Ions in Matter (SRIM) tables (Ziegler et al., 2010) were used to calculate the energy loss of protons in the target. Then the effective energy of the protons in the target was found by iterative calculations using the expression (Angulo et al., 1993)

$$\int_{E_0-\Delta}^{E_0} \sigma(E)\varepsilon(E)^{-1}dE = 2\int_{E_{eff}}^{E_0} \sigma(E)\varepsilon(E)^{-1}dE \qquad (1)$$

where σ(E) is the cross-section of the reaction at the CM Energy E. Here a function σ(E) has been formed at these energies by fitting the data of Ref. (Becker et al., 1987). ε(E) is the stopping power of protons in the target at the CM Energy E. A function has been fitted here too, using the SRIM data. E_0 is the initial CM energy before entering the target. Δ is the energy loss of the beam, E_{eff} is the effective beam energy at the target.

Uncertainty in the effective energy $\Delta(E_{eff})$ is found as 9 keV which is calculated by the expression

$$\Delta(E_{eff}) = \sqrt{\frac{1}{N}\int_{E_0-\Delta}^{E_0}\left(E - E_{eff}\right)^2 \sigma(E)dE} \qquad (2)$$

where N is normalization constant which can be shown as;

$$N = \int_{E_0-\Delta}^{E_0} \sigma(E)dE \qquad (3)$$

Here again, the function used at Eq. (1) has been used as σ(E).

The partial cross-sections at these energies have been calculated using the expression;

$$\sigma(E_{eff}) = 4\pi\,(n_\alpha\, cos\Theta) \,/\, (I\, n_0\, \Omega) \qquad (4)$$

where

$\sigma(E_{eff})$: Partial cross-section at effective CM energy E_{eff}

E_{eff} : Effective CM energy

n_α : Number of alpha particles counted

I : Number of protons arrived at the target

n_0 : Number of ^{11}B nucleus per unit surface (cm^2)

Ω : Solid angle (steradians)

Θ : The angle between the target normal and the beam direction ($\theta = 0^0$)

Two different S-Factor sets have been calculated. The first one is for ^{11}B(p,α_0)^{8}Be channel (Fig.5) which was compared with (Becker et al., 1987), (Spitaleri et al., 2004) and the second one is for ^{11}B(p,α_1)*^{8}Be channel (Fig. 6) which was compared with (Becker et al., 1987), (Angulo et al., 1993).

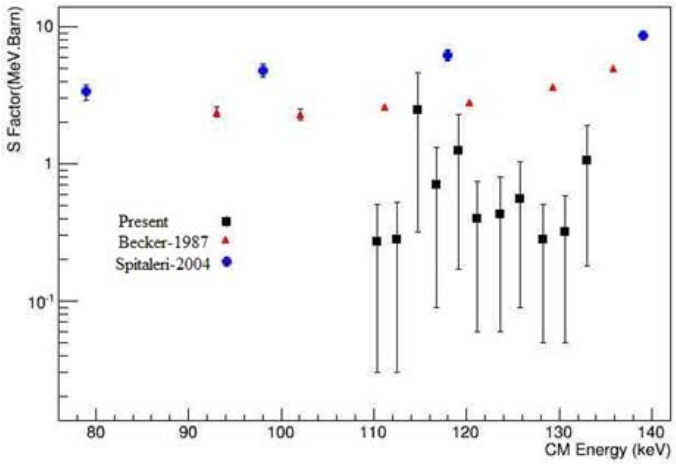

Figure 5. Calculated S-factor of the 11B(p,α0)8Be channel and compared with (Becker et al., 1987), (Spitaleri et al., 2004)

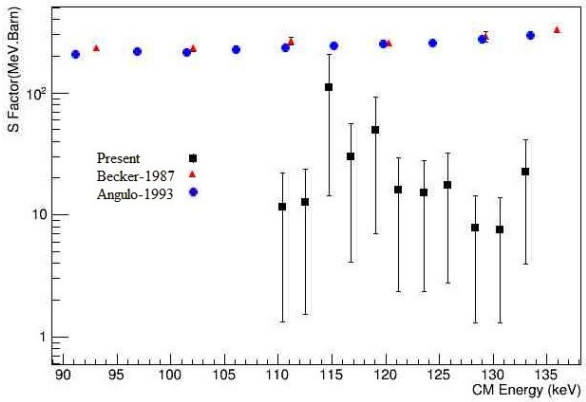

Figure 6. Calculated S-factor of the $^{11}B(p,\alpha_1)^{*8}Be$ channel and compared with (Becker et al., 1987), (Angulo et al., 1993)

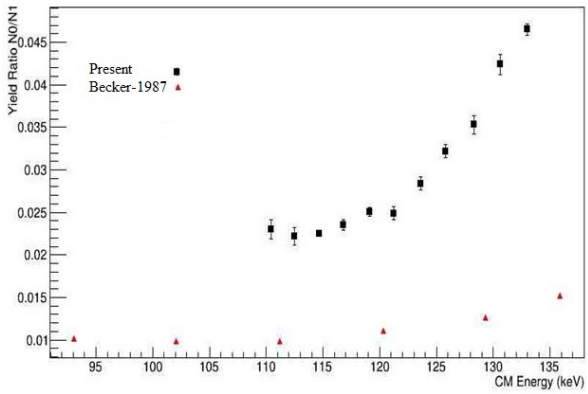

Figure 7. Yield ratio N_0/N_1 of the reaction channels $^{11}B(p,\alpha_0)^8Be$ and $^{11}B(p,\alpha_1)^8Be$.

The S-Factor has been calculated by the expression

$$S(E_{eff}) = \sigma(E_{eff})\ E_{eff}\ exp\,(2\pi\eta) \qquad (5)$$

where

$S(E_{eff})$:S-factor at effective CM energy Eff

η :Sommerfeld parameter

When the S-factor values obtained in this study are compared with the literature values, it is observed that there is a significant difference. It has been evaluated that this may be due to Carbon build-up on the target surface during irradiation. Two factors were effective in reaching this conclusion. First; When the irradiated targets are examined, a brown-black darkening is observed in the irradiated region (Fig.8). Latter; Although the reason could not be understood during the irradiation, it was observed that the number of alpha particles reaching the detector decreased over time and almost no particles came towards the end of the irradiation.

Figure 8. Brown-black darkening in the irradiated region

The particles in the beam lost their energy by passing through this Carbon layer before reaching the ^{11}B nuclei. The calculated effective CM energy may be much less than the actual generated effective CM energy. This may have caused the calculated S-factor values to be less than expected.

When the E_{eff}(CM) values in this study are decreased by about 30 keV (Fig. 9), it is seen that the S-factor values corresponding to these energies are compatible with the values in (Becker et al., 1987). Based on this, it can be said that the proton beam lost about 30 keV of energy before reaching the ^{11}B target. By assuming a Carbon, Hydrogen and Oxygen accumulation on the target with a stoichimetric ratio 3:2:1 respecticely (Healy, 1997) with a stopping power of 0.59 keV/μg/cm^2 this means an average accumulation of 51.28 μg/cm^2. It must be noted that while calculating the 51.28 μg/cm^2 value obtained here, the gradual accumulation of Carbon was neglected, and it was assumed that the proton beam encountered the same Carbon layer thickness throughout the entire irradiation. Therefore, the amount of Carbon deposited at the end of the irradiation is actually more than the average value of 51.28 μg/cm^2.

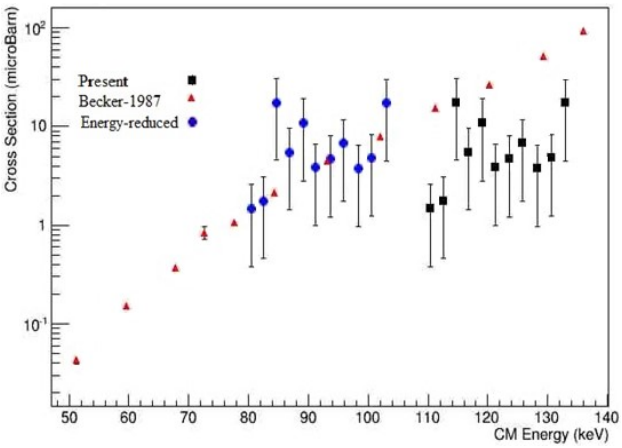

Figure 9. The cross-section data of $^{11}B(p,\alpha_0)^8Be$ reaction. Energy reduced values were compatible with (Becker et al., 1987)

Some calculations were evaluated to see if a Carbon build-up of 51.28 μg/cm^2 was possible. Moller et al., was investigated Carbon deposition on Ni surfaces bombarded with H^+, He^+ and Li^+ ions (Möller et al., 1981). In this study, the authors carried out their experiments at a pressure of 10^{-6} mbar and measured the amount of Carbon deposited on the surfaces using the $^{12}C(d,p)^{13}C$ reaction. In Fig.4 of (Möller et al., 1981), the amount of Carbon accumulation obtained depending on the irradiation dose is given according to different ion types. In the figure:

j : ion current and j/W : the number of ions arrived to the surface per carbon atoms formed.

When the (c) part of the figure is examined, it can be said that roughly one Carbon atom is accumulated for each ion on the surfaces bombarded with H+ ions with 100 keV energy, at irradiation doses up to 0.5x1014 ions/s corresponding to 8 μA. For recent study by using the formulas:

$$N' = {}^{N}/_{S} = N_1\,{}^{t}/_{S} = {}^{(I/e)t}/_{(\pi ab)} \qquad (6)$$

and,

$$d = \frac{1}{3}\left(\frac{N'}{N_A}\right)M \qquad (7)$$

Where;

N: the total number of ions hitting the target during the irradiation

S: the irradiated surface area which is an ellips with dimentions a = 0.25 cm, b = 0.07cm

N_1: The ions arrived the target per unit time

t: the irradiation time (4250 s.)

I: the ion current (5 μA)

e: elementary charge ($1.6*10^{-19}$)

d: thickness of the Carbon accumulation (μg/cm^2)

N_A: Avogadro's number

M: Molar mass of the C_3H_2O (54 g/mole)

It can be found that the number of ions per unit surface and consequently the number of Carbon atoms accumulated on the target is N'=$2.42*10^{18}$ atoms/cm^2 which corresponds to a thikness of d=72.36 μg/cm^2. This value is greater than 51.28 μg/cm^2 value. But as it be noted before, 51.28 μg/cm^2 is not the final thickness but the average thickness, the protons encountered. Of course the final thickness is actually greater than the average one.

Yield ratio N_0/N_1 of the reaction channels $^{11}B(p,\alpha_0)^8Be$ and $^{11}B(p,\alpha_1)^8Be$ is given in (Fig. 7). It seems N_0/N_1 values obtained in present work are greater than those of (Becker et al., 1987). To calculate N_1 we have taken one third of total number of α_1, α_{11} and α_{12}. But α_{11} and α_{12} particles have less energy compared to α_0 particles. Hence these particles can easily be absorbed by the Carbon layer and the number of α_{11} and α_{12} particles arrived to the detector be decreased, which can effect N_1 negatively, while the number of α_0 particles (N_0) have been unaffected. That is why N_0/N_1 obtained in this study is greater than that of (Becker et al., 1987).

4. Conclusions

It was observed that there was a significant difference between the S-factor values measured in this work and the literature values. The reason for these differences was considered to be Carbon build-up on the target surface during irradiation. On average, it has been calculated that the proton beam encounters a Carbon build-up of 51.28 μg/cm2 before reaching the target.

When the alpha spectra are examined, it can be said that the cross-section of the $^{11}B(p,\alpha_0)^8Be$ reaction channel increases with beam energy faster than that of $^{11}B(p,\alpha_1)^8Be$. In this study, it has been found that the yield ratio N_0/N_1 of the reaction channels $^{11}B(p,\alpha_0)^8Be$ and $^{11}B(p,\alpha_1)^8Be$ is greater than that of literature. This result is attributed to that the alpha particle (α_{11}, α_{12}) energies of the $^{11}B(p,\alpha_1)^8Be$ reaction channel is small, so that some of them can't penetrate out of the Carbon layer and can't arrive the detector which decreases N_1 and consequently increases N_0/N_1.

Acknowledgments

This study was supported by the Turkish Energy, Nuclear, and Mineral Agency with Project Code A2.H4.F3.

References

1) Alaçayır, O. (2015). Measurement of Partıal Differential Cross Sections of the 11B(p,α)2α Reaction Occured by Bombardıng B2O3 Target wıth 103-127 keV Protons. MSc. Thesis, Istanbul Technical University.
2) Amersham. (1992). Certificate of calibration of alpha emitting radioactive reference source. A 3583(Calibration No: 0146).
3) Angulo, C., Engstler, S., Raimann, G., Rolfs, C., Schulte, W. H. & Somorjai, E. (1993). The effects of electron screening and resonances in (p, α) reactions on10B and11B at thermal energies. Zeitschrift Für Physik A Hadrons and Nuclei, 345(2), 231–242. https://doi.org/10.1007/BF01293350.
4) Baykal, A. (1997). Li+d reaction at low energies. Doctorate Thesis, Istanbul University.
5) Becker, H. W., Rolfs, C. & Trautvetter, H. P. (1987). Low-energy cross sections for11B(p, 3α). Zeitschrift Für Physik A Atomic Nuclei, 327(3), 341–355. https://doi.org/10.1007/BF01284459.
6) Belyaev, V. S., Krainov, V. P., Matafonov, A. P. & Zagreev, B. V. (2015). The new possibility of the fusion p $\mathplus$11B chain reaction being induced by intense laser pulses. Laser Physics Letters, 12(9), 96001. https://doi.org/10.1088/1612-2011/12/9/096001.
7) Boesgaard, A. M., Deliyannis, C. P. & Steinhauer, A. (2005). Boron Depletion in F and G Dwarf Stars and the Beryllium-Boron Correlation. The Astrophysical Journal, 621(2), 991–998. https://doi.org/10.1086/427687.
8) Davidson, J. M., Berg, H. L., Lowry, M. M., Dwarakanath, M. R., Sierk, A. J. & Batay-Csorba, P. (1979). Low energy cross sections for 11B(p, 3α). Nuclear Physics, Section A, 315(1–2), 253–268. https://doi.org/10.1016/0375-9474(79)90647-X.
9) Healy, M. J. F. (1997). Minimising carbon contamination during ion beam analysis. Nuclear Instruments and Methods in Physics Research Section B: Beam Interactions with Materials and Atoms, 129(1), 130–136. https://doi.org/https://doi.org/10.1016/S0168-583X(97)00127-4.
10) Kokkoris, M., Kafkarkou, A., Paneta, V., Vlastou, R., Misaelides, P. & Lagoyannis, A. (2010). Differential cross sections for the 11B(p,αo) 8Be and 11B(p,p0)11B reactions, suitable for ion beam analysis. Nuclear Instruments and Methods in Physics Research, Section B: Beam Interactions with Materials and Atoms, 268(24), 3539–3545. https://doi.org/10.1016/j.nimb.2010.09.013.
11) Lamia, L., Spitaleri, C., Burjan, V., Carlin, N., Cherubini, S., Crucillà, V., Munhoz, M. G., Santo, M. G. Del, Gulino, M., Hons, Z., Kiss, G. G., Kroha, V., Kubono, S., Cognata, M. La, Li, C., Mrazek, J., Mukhamedzhanov, A., Pizzone, R. G., Puglia, S. M. R. & Zhou, S. H. (2011). New measurement of the11B(p,$\upalpha$0)8Be bare-{nucleusS}(E) factor via the Trojan horse method. Journal

of Physics G: Nuclear and Particle Physics, 39(1), 15106. https://doi.org/10.1088/0954-3899/39/1/015106.
12) Mayer, M., Annen, A., Jacob, W. & Grigull, S. (1998). The 11B(p,α0)8Be nuclear reaction and 11B(p,p)11B backscattering cross sections for analytical purposes. Nuclear Instruments and Methods in Physics Research, Section B: Beam Interactions with Materials and Atoms, 143(3), 244–252. https://doi.org/10.1016/S0168-583X(98)00383-8.
13) Möller, W., Pfeiffer, T. & Schluckebier, M. (1981). Carbon buildup by ion-induced polymerization under 100-400 keV H, He and Li bombardment. Nuclear Instruments and Methods, 182–183(PART 1), 297–302. https://doi.org/10.1016/0029-554X(81)90703-5.
14) Oliphant, M. L. E. & Rutherford, Lord. (1933). Experiments on the Transmutation of Elements by Protons. Proceedings of the Royal Society of London. Series A, Containing Papers of a Mathematical and Physical Character, 141 (843), 259–281. http://www.jstor.org/stable/96218.
15) Spitaleri, C., Lamia, L., Tumino, A., Pizzone, R. G., Cherubini, S., Del Zoppo, A., Figuera, P., La Cognata, M., Musumarra, A., Pellegriti, M. G., Rinollo, A., Rolfs, C., Romano, S. & Tudisco, S. (2004). The 11B(p, α0)8Be reaction at sub-Coulomb energies via the Trojan-horse method. Physical Review C-Nuclear Physics, 69 (5), 1–11. https://doi.org/10.1103/PhysRevC.69.055806.
16) Stave, S., Ahmed, M. W., France, R. H., Henshaw, S. S., Müller, B., Perdue, B. A., Prior, R. M., Spraker, M. C. & Weller, H. R. (2011). Understanding the B11(p,α)αα reaction at the 0.675 MeV resonance. Physics Letters, Section B: Nuclear, Elementary Particle and High-Energy Physics, 696(1–2), 26–29. https://doi.org/10.1016/j.physletb.2010.12.015.
17) Tarcan, G., Subaşı, M., Özbir, Y. & Baykal, A. (1998). J-15 Hızlandırıcısının Yeniden Kazanılması. CNAEM Report, TR-335.
18) Wessel, F. J., Binderbauer, M. W., Rostoker, N., Rahman, H. U. & O'Toole, J. (2000). Colliding beam fusion reactor space propulsion system. AIP Conference Proceedings, 504(1), 1425–1430. https://doi.org/10.1063/1.1290961.
19) Whitcher, R. (2014). SaCalc-Ellipsoid. http://www.oecd.nea.org/tools/abstract/detail/nea-1884.
20) Ziegler, J. F., Ziegler, M. D. & Biersack, J. P. (2010). SRIM - The stopping and range of ions in matter (2010). Nuclear Instruments and Methods in Physics Research, Section B: Beam Interactions with Materials and Atoms, 268(11–12), 1818–1823. https://doi.org/10.1016/j.nimb.2010.02.091.

Turkish Journal of Nuclear Science (2022), Vol. 34, No.1. Page:16-32. http://dergipark.gov.tr/tjins

TENMAK TURKISH ENERGY, NUCLEAR AND MINERAL RESEARCH AGENCY

TURKISH JOURNAL OF NUCLEAR SCIENCES

Journal homepage https://dergipark.org.tr/tr/pub/tjns

INFLUENCE OF PRE-RADIATION-OXIDIZING TREATMENT ON THE SPECIFIC RESISTANCE OF ZIRCONIUM

Teymur AGAYEV, Gunel IMANOVA*, Anar ALİYEV

Institute of Radiation Problems, Azerbaijan National Academy of Sciences,

AZ 1143 - Baku, Azerbaijan

* gunel_imanova55@mail.ru

Abstract:

The effect of preliminary radiation-oxidative treatment on the relative change in the resistance ($\Delta\rho$ / $\Delta\rho 0$) of metallic zirconium has been studied. The contribution of preliminary radiation-oxidative treatment to the change in the electro physical characteristics during thermal and radiation-thermal tests in the contact of zirconium with water is revealed. The effect of preliminary radiation-oxidative treatment on the current density and current-voltage characteristic of metallic zirconium has been studied. The completion of the protective oxide film during the radiation-oxidative treatment of zirconium (D≥80 kGy) is accompanied by a decrease in electrical conductivity and current values in the study of their current-voltage characteristics. When these samples are tested in the processes of radiation-thermal and thermal decomposition of water, a partial destruction of the protective oxide film occurs as a result of which additional charge carriers accumulate on the surface. The rate of destruction of the surface oxide film and the accumulation of charge carriers during radiation-thermal processes are higher than during thermal processes.

Keywords: Metallic zirconium; γ-radiation; current-voltage characteristics; electro-physical; radiation-oxidatively.

1.Introduction

Radiation-heterogeneous processes in contact of preliminarily radiation-oxidative treated zirconium with water causes a change in the amount of surface oxide film. The formation of an oxide film, in turn, changes the radiation-catalytic activity and physicochemical properties, which affect the kinetic parameters. One of them, the most sensitive is the electro physical and optical properties of metal surfaces. Therefore, after testing zirconium samples in the process of water decomposition, the study of the electro physical and optical properties is of great interest (Liu and Han, 2022; Zhu et al., 2016; Ma, Yuan & Sehgal, 2016; Wang et al., 2021; Frano, Ciolini & Pesetti, 2020; Du, Bernat & Jay Gerin, 2000; Kang et al., 2009; Guello et al., 2000; Amblard et al., 2006).

The study of the kinetics of radiation, radiation-thermal and thermal processes shows that in metals used directly in a nuclear reactor, there is not only a change in natural defect states, but also the appearance of new defects - displaced interstitial atoms, as well as a change in surface properties due to adsorption, insertion other substances (for example O_2, H_2), corrosion, etc.

As is known, the accumulation of point defects and impurities introduced during irradiation (for example, O_2, H_2) strongly affect the physical properties of the metal (Zongyang et al., 2021). Thus, a consistent study of the physical properties before and after thermal and radiation-thermal treatment makes it possible to judge changes in electronic and structural defects and draw certain conclusions about the processes taking place (Garibov et al., 1992; Garibov, 2004; Garibov, 2005; Imanova, Agayev & Jabarov, 2021; Ali et al., 2021; Imanova & Hasanov, 2020; Imanova, 2021; Agayev, Musayeva & Imanova, 2021; Imanova, 2020; Imanova et al., 2021).

The purpose of this work is to change the resistance and thermo EMF. metallic zirconium, occurring in samples pretreated and tested under conditions of radiation-thermal and thermal effects. The purpose of this work is to change the current density and current-voltage characteristic of metallic zirconium, which occur in samples pretreated and tested under conditions of radiation-thermal and thermal effects.

2. Experimental

Investigated plates of reactor zirconium (purity 99.99%) with a thickness of d = 0.012 - 0.20 mm; width b = 2.0 - 4.0 mm and length l = 20 - 25 mm. The samples were preliminarily cleaned with ethyl alcohol, acetone and distilled water, dried first in air, then in vacuum ($1 \cdot 10^{-3}$ Pa) at T = 300 K, and then at T = 473 K. Then the samples were placed in ampoules with 30% - solution of hydrogen peroxide (CH_2O_2 = 9 mol/L) and subjected to preliminary exposure to gamma rays (absorbed dose rate D = 1.14 Gy / s) at different exposure times. Then the samples were dried and their electro physical parameters were measured. Then the samples were placed in special ampoules to test their radiation-catalytic activity in the processes of radiolysis decomposition of water. The required amount of water was introduced into ampoules with samples by condensation of water vapor from a graduated volume of a vacuum adsorption unit. The accuracy of introducing water into ampoules with samples from a vacuum adsorption installation in the investigated range of water vapor density values was ± 5%. During the experiments, the temperature was maintained with an accuracy of ± 1^0C. Radiation-oxidative treatment and radiation-thermal tests were carried out on an isotope source of γ-radiation ^{60}Co. Dosimetry of the source was carried out with chemical dosimeters - ferrosulfate, cyclohexane and methane. Measurements of electrical resistivity and measurement of current-voltage characteristics were carried out using four probe point contacts by the method of compensation at constant voltage (Gunel & Kaya, 2021). We used power supplies of the TES-41 brand, a universal voltmeter of the V7-21 and V7-21A brands (for measuring the voltage drop), and a combined digital device Sh4313 (for measuring current).

The electro-physical properties of samples subjected to preliminary radiation-oxidative treatment were also determined under conditions of radiation-thermal and thermal tests in contact with a heat transfer water (density ρ=5 mg/cm^3) at T=673K, D=1.14 Gy/s.

The kinetics of radiation decomposition of hydrogen peroxide in aqueous solutions has been studied in many works. Some of the dependencies established in them are consistent with each other. At the same time, there are some discrepancies. In (Imran et al., 2022; Gunel, 2022; Imran et al., 2020; Murat et al., 2021; Hokman et al., 2021), the kinetics of the reaction of radiation decomposition of hydrogen peroxide under the action of radiation in the concentration range 0.5-18 mol $\cdot L^{-1}$ was investigated. At concentrations up to 4 mol $\cdot L^{-1}$, the reaction was first order with respect to hydrogen peroxide; at concentrations above 4 mol$\cdot L^{-1}$, the reaction order is higher. The reaction rate is proportional to the square root of the radiation intensity; the activation energy is 5.1 kcal$\cdot$mol^{-1}.

In the radioactive decomposition of H_2O_2, ions play a certain role. Based on this, the following process scheme was proposed;

*Corresponding author: Gunel IMANOVA, Institute of Radiation Problems, Azerbaijan National Academy of Sciences, AZ 1143 - Baku, Azerbaijan E-mail: gunel_imanova55@mail.ru : Gönderim: 21/02/2022 Kabul: 06/07/2022.

$$H_2O_2 \rightarrow 2\dot{O}H$$
$$\dot{O}H + H_2O_2 \rightarrow H_2O + H\dot{O}_2$$
$$H\dot{O}_2 + H_2O \rightarrow H_3O^+ + O_2^-$$
$$H_2O_2 + O_2^- \rightarrow HO^- + \dot{O}H + O_2$$
$$H_2O_2 + H\dot{O}_2 \rightarrow H_2O + O_2 + \dot{O}H$$
$$\dot{O}H + H\dot{O}_2 \rightarrow H_2O + O_2$$

Since the radical is inactive, the reaction should proceed relatively slowly. The reaction processes should proceed quickly, since the transitions of the proton and the electron proceed without a significant energy barrier.

3. Results and discussion

The paper presents the results of a study of changes in the electrophysical properties of preliminarily radiation-oxidatively treated zirconium samples as a result of their testing during thermo- and thermoradiolytic processes of water decomposition. At the same time, special attention is paid to the following aspects;

- ✓ During the operation of radiation-oxidatively treated zirconium samples under real operating conditions of water-cooled nuclear reactors, all parameters of these samples change, including surface physicochemical parameters, corrosion resistance, and electrical properties. A special place in the change of these properties belongs to the processes of defect formation in the Zr-ZrO_x system.
  The study of changes in the electrophysical properties of pretreated zirconium samples allows us to judge the mechanism of defect formation and, ultimately, about all radiation-heterogeneous processes in the Zr-ZrO_x-H_2O system. Therefore, we have carried out studies of changes in resistivity-, thermo emf- of preliminarily radiation-oxidatively treated zirconium samples after testing them in contact with water at T = 673K, at various absorbed doses.
- ✓ The current-voltage characteristics of these samples were studied in order to clarify the state and quantitative features of charge carriers formed in the Zr-ZrO_2 system under the influence of radiation-heterogeneous processes in contact with water.

Based on the experimental results, generalizations are made about the mechanism of defect formation and their effect on the electrophysical properties of the Zr-ZrO_2 system.

When irradiated with γ-quanta, which create damage in metals and alloys, complex processes occur that lead to the formation of defect structures in the form of electronic and lattice defects, pores, precipitates, etc. This is the reason for the application of the method of resistivity and thermoelectric power (Agayev, Imanova & Imran, 2021; Gunel & Bekpulatov, 2021; Sami & Imanova, 2022; Imran & Imanova, 2022). Publications in recent years indicate an increased attention to this method, due to its high sensitivity to smaller defect structures and in solving many problems in damage physics and radiation materials science.

In the present work, are investigated the possibilities of methods for studying the resistivity (Δρ / Δρ0) and thermo-emf (α) in the study of the processes of radiation oxidation of the surface of zirconium in contact with H_2O_2. During the radiation-oxidative treatment of metals, an oxide phase is formed on the surface, which affects the resistivity of materials. Therefore, electrophysical methods began to be widely used as a method for obtaining information on the state of structural materials in nuclear technologies.

Figure 1 shows the dependences of the resistivity of preliminarily radiation-oxidatively treated samples on the time of γ-irradiation at. As can be seen from the figure, at low values of the absorbed dose D≤20kGy, the resistivity of the samples decreases in comparison with the initial state. The observed decrease in the resistivity in the initial regions of the time of radiation-oxidative treatment of zirconium is associated with surface radiation-heterogeneous processes. In the initial doses of radiation-oxidative treatment of zirconium, there is an accumulation of defect states in the surface oxide phase.

When irradiated with γ-quanta, which create damage in metals and alloys, complex processes occur that lead to the formation of defect structures in the form of electronic and lattice defects, pores, precipitates, etc. This is the reason for the application of the method of resistivity and thermo-emf (Barkaoui et al., 2022). Publications in recent years indicate an increased attention to this method, due to its high sensitivity to smaller defect structures and in solving many problems in damage physics and radiation materials science.

In the present work, the possibilities of methods for studying the resistivity (Δρ / Δρ0) and thermo-emf are investigated. In the study of the processes of radiation oxidation of the surface of zirconium in contact with H_2O_2. During the radiation-oxidative treatment of metals, an oxide phase is formed on the surface, which affects the resistivity of materials. Therefore, electrophysical methods began to be widely used as a method of obtaining information on the state of structural materials of nuclear technologies.

Figure 1 shows the dependences of the resistivity of preliminarily radiation-oxidatively treated samples on the time of γ-irradiation at. As can be seen from the figure, at small values of the absorbed dose D≤20kGy, the resistivity of the samples decreases compared to the initial state. The observed decrease in the resistivity in the initial regions of the time of radiation-oxidative treatment of zirconium is associated with surface radiation-heterogeneous processes. In the initial doses of radiation-oxidative treatment of zirconium, there is an accumulation of defect states in the surface oxide phase:

$$Zr\text{-}ZrO_x \rightarrow Zr\cdot ZrO^*$$

where - Zr-ZrOx is the initial state of the surface with a protective oxide phase, $Zr\cdot ZrO^*$ is the defect state formed as a result of the action of γ-quanta (the defect state can be attributed to the localized state of nonequilibrium charge carriers, vacancies of anions, surface O- holes) .

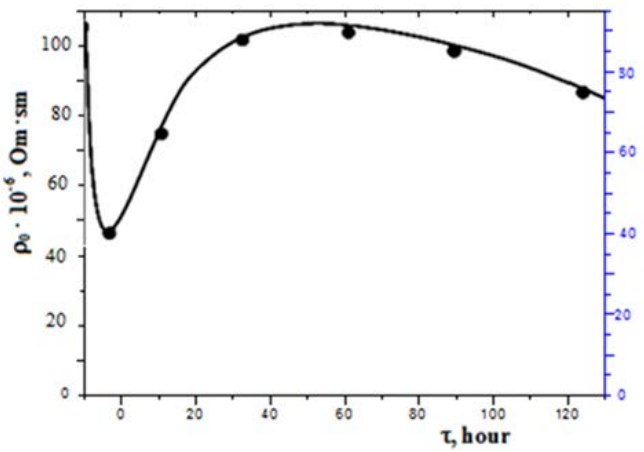

Figure 1. Dependence of the resistivity of zirconium samples on the time of preliminary irradiation at T = 300K, D=1.14 Gy/s in an H_2O_2 medium.

As a result of the interaction of surface defect states with the products of H_2O_2 radiolysis, hydroxyl-containing states of zirconium atoms are formed and dissolved in the contacting medium. Partial destruction of the biographical oxide film and the formation of charged states lead to a decrease in the resistivity of the metal. With a further increase in the time of radiation-oxidative treatment, an oxide film is formed. As a result of the interaction of charged and coordination-unsaturated metal atoms by the products of H_2O_2 radiolysis, a new oxygen-containing state of the zirconium surface is formed.

After D≥123 kGy, the predominance of the formation of the oxide phase begins during radiation-heterogeneous processes in the Zr-H_2O_2 system, therefore, the resistivity of the radiation-oxidatively treated samples begins to increase.

The obtained results show that a stable protective oxide film can be formed in a certain amount on the zirconium surface. Its properties depend on the methods of its formation. It was revealed that a stable state of a protective oxide film is formed on the surface of zirconium during radiation-oxidative treatment. The stability of the surface oxide state remains in the range of values of the absorbed radiation dose D≈123 ÷ 290 kGy. The observed decrease in the resistivity of the samples preliminarily radiation-oxidatively treated in an H_2O_2 medium in the

region of the absorbed radiation dose D≥290 kGy is apparently associated with the accumulation of stable charged states in the Zr-ZrOx system.

In order to elucidate the nature of the dependence of the resistivity ρ(τ) on the preliminary oxidative treatment of the metal surface, the relative change in the resistance and thermo emf of the samples preliminarily radiation-oxidatively treated at times corresponding to a minimum (5 hours) was studied.

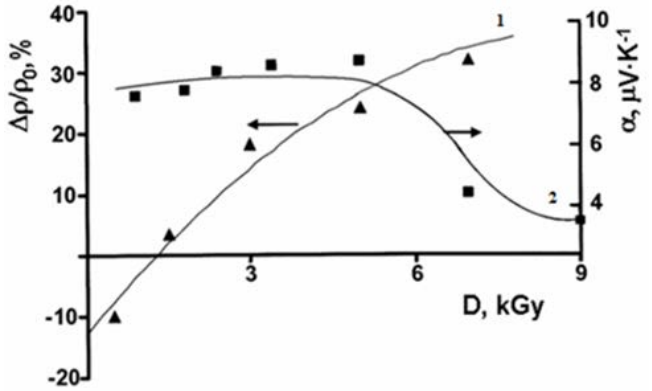

Figure. 2. Dependence of Δρ / Δρ0 = f (D) and α = f (D) of metallic zirconium (Zr) on the absorbed dose.

Figure 2. (curve 1) shows the dependences of the relative change in resistance Δρ / Δρ0 and thermo-emf (α) of radiation-thermally tested plates on the absorbed radiation dose. It can be seen from the figure that Δρ / Δρ0 initially decreases and at low doses increases intensively, and at relatively large doses (D≥3.5 kGy) the growth of Δρ / Δρ0 weakens and slowly approaches saturation.

As a result of the interaction, Zr-ZrO_2 appears, the localization of which proceeds until the surface is saturated with them. The relative resistance in the samples after the radiation-heat treatment slowly increases (Fig. 2, curve 1), and the value of the thermo-emf (curve 2) decreases. As is known, the thermo emf (α) is very sensitive to changes in the Fermi properties of the metal surface and therefore, by measuring the thermo emf of the samples, we obtain additional information on the localization of charge carriers and the defectiveness of the tested samples. With an increase in the absorbed dose D>50 kGy, the value of thermoelectric power decreases, which directly confirms an increase in the concentration of emitted charge carriers.

The article presents the results of experimental studies by measuring the current-voltage characteristics (CVC) of zirconium plates, pre-irradiated in an H_2O_2 medium at various doses, and then tested in the process of radiation-thermal and thermal decomposition of water at T=673K, $\rho_{H_2O} \approx 5mG/sm^3$,$\dot{D} = 1.14Gy/s$.

As is known, the appearance on the metal surface of various point defects, vacancies and surface oxidation processes strongly affect the metal conductivity. To identify certain factors affecting the conductivity of metallic zirconium, we studied the current-voltage characteristics (CVC) and changes in the current density of thin zirconium plates 80-200 μm thick, depending on the absorbed dose of gamma quanta.

Figure 3 (τ=5 hour) shows the CVC characteristics of the initial (curve a), pre-irradiated (curve b) in an H_2O_2 medium at T=300K, τ = 5hour., $\dot{D} = 1.14Gy/s$. samples of zirconium plates and CVC characteristics of the same samples tested in the process of thermal (curve c) and radiation-thermal (curve d) decomposition of water at T=673K, τ= 30 min, $\rho_{H_2O} \approx 5mG/sm^3$.

The figure shows that at the same electric voltage (for example, at U=8·10^{-5} V/sm), the current increases by

$\frac{J_{pr.}-J_0}{J_0} = \frac{9-3,4}{3,4} = 1,45$; $\frac{J_T-J_{0.}}{J_0} = \frac{7-3,4}{3,4} = 1,06$ and $\frac{J_{RT}-J_{0.}}{J_0} = 0,15$.

where: J_0 - is the current strength of the original samples, $J_{pr.}$ - current strength of pre-irradiated samples, J_T and J_{RT} - current strength of the same samples thermally and radiation-thermally tested in the process of water decomposition. As can be seen from the figures, to obtain the same current strength, for example J = 4·10^{-3}A, the following electric voltages will be required accordingly: for the initial sample 10.5·10^{-5} V, for the preliminary radiation-oxidative treated sample (curve b) - 3, 5·10^{-5} V, i.e. almost three times less, for a preliminary radiation-oxidatively treated sample tested at thermal (curve c) 9.5·10^{-5} V and radiation-thermal U = 4.5·10^{-5} In the processes of water decomposition, i.e. approximately 2.3 times less.

Hence, it can be seen that when measuring a preliminarily radiation-oxidatively treated zirconium sample and the same sample after testing in the process of radiation-thermal decomposition of water to obtain the same current, the applied electric voltages decrease by almost 3 and 2.3 times, respectively. This is due to an increase in the concentration of current carriers.

Figure 3 (τ=15 hour) shows the I - V characteristics of the same conditions at the time of preliminary irradiation with gamma quanta $\tau_{irra.}$=15 hours, where it is shown that there is a change in the current strength in the same value of the electric voltage (U=8·10^{-5} V/sm). As can be seen after thermal and radiation-thermal tests, the J of the samples increases during the decomposition of water. It can be seen from the figure that the properties of the CVC characteristics of preliminarily radiation-oxidatively treated samples strongly depend on the absorbed dose of γ-quantum, since in the sample irradiated during τ= 15 hours at the same electrical voltage (eg U=8·10^{-5}V) J - the current decreases $\frac{(J)_{\tau=5}}{(J)_{\tau=15}} = \frac{9\cdot10^{-5}}{3,5\cdot10^{-5}} \approx 2,5$times. In the samples tested in radiation-thermal processes, J (U) changes in the same way as in the samples pre-irradiated during τ = 15 hours.

From Figure 3 (τ=30 hour) where the CVC characteristics of the above processes are shown: a - initial samples; b - pre-irradiated in an H_2O_2 environment; c - thermally and d - radiation-thermally tested samples, it can be seen that the current strength of the samples after preliminary irradiation in an H_2O_2 medium at an irradiation time $\tau_{irra.}$=30 h., increased by 14.7%, and after the thermal test by 29.4% and, accordingly, after the radiation-thermal test, it doubled.

With a further increase in the pre-irradiation time, similar results were obtained.

Figure 3 (τ=50 hour) also shows the results of studies of the CVC characteristic in the same sequence of zirconium samples preliminarily radiation-oxidatively treated (curve b) in an H_2O_2 medium during sample. τ=50 hours and the same samples tested in the processes of thermal (curve c) and radiation-thermal (curve d) decomposition of water (T = 673K, τ= 30 min, $\rho_{H_2O} \approx 5mG/sm^3$).

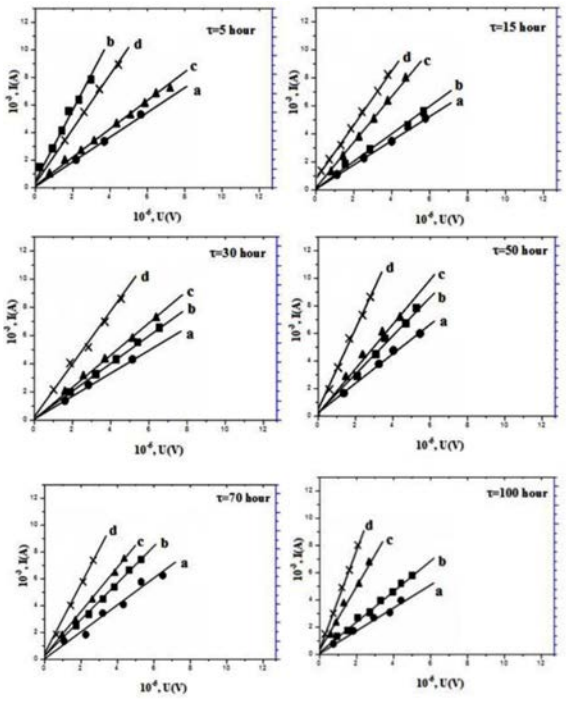

Figure 3. Current-voltage characteristic of zirconium samples: t=5, 10, 30, 50, 70 and 100 hours, D =1.14Gy/s

a- original sample

b- preliminarily irradiated sample in H_2O_2 medium at T=300K

c- thermally and

d-radiation-thermally tested samples after preliminary irradiation in H_2O_2 environment.

It can be seen from the figure that at the same electric voltage, the current strength of the samples tested in thermal and radiation-thermal processes, respectively, increases by $2.1 \cdot 10^{-2}$ and U=$6.6 \cdot 10^{-2}$ A, i.e. increases approx. 1.7 and 2.2 times.

Figure 3 (τ=70 hour) shows the CV characteristics of the initial (a) samples and the CV characteristics of the same samples tested in the process of thermal (c) and radiation-thermal (d) decomposition of water after their preliminary irradiation in an H_2O_2 medium at T=300K for τ= 70 hours. As can be seen from the figure, after preliminary irradiation, the current increased by 8.94%. After heat treatment of the same samples in the process of water decomposition, the current increased by 26.5% (Fig. 3 (τ=70 hour), curve c), and after the radiation-thermal process, it increased by 1.5 times (curve d), i.e. the current strength increased by the same percentage.

Figure 3 (τ=100 hour) also shows the CV characteristics of the initial (a) samples and the CV characteristics of the same samples tested in the process of thermal (c) and radiation-thermal (d) decomposition of water (T=673K, $\rho_{H_2O} \approx 5mG/sm^3$, $\dot{D} = 1.14Gy/s$) after their preliminary irradiation in an H_2O_2 medium at T=300K for τ=100 hours. As can be seen from the figure, under these conditions, the CV characteristics of the samples are very different from the previous ones. It was revealed that the current strength of the thermally treated samples increased by ≈35.5% and in the samples tested during radiation-thermal processes almost 3 times.

Comparison of the results of the study $\sigma=f(D_{irra.})$ and the current-voltage characteristic shows that there are satisfactory coincidences between them. Since during radiation-oxidative treatment at low values of the irradiation dose D≤20-25 kGy, charged states are formed and the samples have a relatively high electrical conductivity. These samples are characterized by a relatively high concentration of charge carriers. Therefore, at the same voltage values, the values of the current strength of the samples preliminarily radiation-oxidatively treated at D≤20-25 kGy are higher than others. With a further increase in the absorbed radiation dose of radiation-oxidative treatment, a protective oxide film is formed and therefore the current strength of the samples processed at the values of the radiation dose D≥30 kGy is less than that of the samples tested during thermal and radiation-thermal processes of water decomposition (Fig. 3).

After testing the zirconium samples preliminarily radiation-oxidatively treated at D≥25 kGy in the processes of radiation-thermal and thermal decomposition of water, the protective oxide film is partially destroyed and, as a result, charged states are formed, which cause an increase in the current strength. The concentration of charge carriers in the samples tested during the radiation-thermal process of water decomposition is higher than that in the samples tested during the thermal process of water decomposition. Therefore, the current strength of these samples in all ranges of values of the radiation dose is greater than that of the original, radiation-oxidative treated and samples tested during thermal processes of water decomposition.

4. Conclusions

The completion of the protective oxide film during the radiation-oxidative treatment of zirconium (D≥80 kGy) is accompanied by a decrease in electrical conductivity and current values in the study of their current-voltage characteristics. The rate of destruction of the surface oxide film and the accumulation of charge carriers during radiation-thermal processes are higher than during thermal processes. Analyzing the results of studies of the electrophysical properties of the initial, radiation-oxidatively treated and tested during radiation-thermal and thermal processes of water decomposition of zirconium samples, the following conclusion can be drawn. When these samples are tested in the processes of radiation-thermal and thermal decomposition of water, a partial destruction of the protective oxide film occurs as a result of which additional charge carriers accumulate on the surface. The rate of destruction of the surface oxide film and the accumulation of charge carriers during radiation-thermal processes are higher than during thermal processes.

References

1) Liu, R. & Han., K. (2022). Experimental study on surface reaction during water injection on molten Zr/Fe pool. Nuclear Materials and Energy. 31. 101176.

2) Zhu, D., Xiang, Q., Zhang, M., Deng, C., Deng, J., Jiang, G., & Yu, H. (2016). Evaluation of in-vessel corium retention margin for small modular reactor ACP100 Annals of Nuclear Energy. 94. 684-690.

3) Ma, W., Yuan, Y., & Sehgal, B. (2016). In-Vessel Melt Retention of Pressurized Water Reactors: Historical Review and Future Research Needs Engineering. 2 (1). 93-111.

4) Wang, H., Villanueva, W., Chen, Y., Kulachenko, A., & Bechta, S. (2021). Thermo-mechanical behavior of an ablated reactor pressure vessel wall in a Nordic BWR under in-vessel core melt retention. Nuclear Engineering and Design. 379. 111196.

5) Lo Frano, R., Ciolini, R., & Pesetti, A. (2020). Analysis of feasibility of a new core catcher for the in-vessel core melt retention strategy. Progress in Nuclear Energy. 123. 103321.

6) Marie Josee, D.P., Philippe, B & Jean Paul, J.G. (2000). Radiolisis of liquid water at temperatures up to 300^0C, A Monte-Carlo simulation. The Journal of Physical Chemistry. 11757-11770.

7) Kang, K.H., Park, R.J., Kim, S.B., & Hong, S.W. (2009). Experimental Study on the Boiling Heat Removal at the Upper Surface of the Metallic Layer During Late-Phase Coolant Injection. Nuclear Technology. 167 (1). 211-222.

8) Guello, J., Fernandez, A., Aurelio, G., & Campo, J. (2000). Metastable structures, bonding properties and phase transitions in alloys of the Zr-Nb and Ti-V systems, 19th European Crystallographic Meeting. Nancy. 422.

9) Amblard, M., Delhaye, M., Froment, K., Seiler, M., & Tourniaire, B. (2006). Consequences of Different Types of Contact Between Water and Molten Steel: The ANAIS Experiments. Nuclear Technology. 153 (3). 315-325.

10) Zongyangç L., Huajian, C., Fangfang, F., Kun, H., Botao, H., & Lian, C. (2021). Experimental Study on Heat Transfer Characteristics of Water Injection on Molten Pool with Low Mass Fraction of Zirconium. Proceedings of the ASME 2021 28th International Conference on Nuclear Engineering August 4-6.

11) Garibov, A.A., Krasnoshtanov, V.F., Agaev, T.N., & Velibekova, G.Z. (1992). The effect of radiation in heterogeneous processes in contact of zirconium and Zr + 1% Nb alloy with water. High energy chemistry. 125-129.

12) Garibov, A.A. (2004). Influence of preliminary radiation-oxidizing treatment on the corrosion resistance of zirconium in conditions of ionizing radiation. Eurasia nuclear bulletin. 45-51.

13) Garibov, A.A. (2005). Effect of preliminary radiation-oxidative treatments coring of zirconium for its radiation-catalytic activity in the processes of water radiolysis. Azerbaijan Chemical Journal. 178-181.

14) Imanova, G.T., Agayev, T.N., & Jabarov, S.H. (2021). Investigation of structural and optical properties of zirconia

dioxide nanoparticles by radiation and thermal methods, Modern Physics Letters B. 2150050-14.

15) Ali, I., Imanova, G.T., Garibov, A.A., Agayev, T.N., Jabarov, S.H., Almalki, A.SA., & Alsubaie, A. (2021). Gamma rays mediated water splitting on nano-ZrO_2 surface: Kinetics of molecular hydrogen formation, Radiation Physics and Chemistry. 109431.

16) Imanova, G.T., & Hasanov, S.H. (2020). Observation the initial radiation to the surface of mixed nano catalyst on oxidation processes, International Journal of Scientific and Engineering Research. 869-873.

17) Imanova, G.T. (2021). Gamma Rays Mediated Hydrogen Generation By Water Decomposition On Nano-ZrO_2 Surface, Modern Approaches on Material Science. 508-514.

18) Agayev, T.N., Musayeva, Sh.Z., & Imanova, G.T. (2021). Studying the Kinetics of Formation of Molecular Hydrogen during the Radiolysis of Hexane and a Mixture of C_6H_{14}–H_2O on a Surface of n-ZrO_2. Russian Journal of Physical Chemistry A. 270–272.

19) Imanova, G.T. (2020). Kinetics Of Radiation-Heterogeneous And Catalytic Processes Of Water In The Presence Of Zirconia Nanoparticles. Advanced Physical Research. 94-101.

20) Imanova, G.T., Agaev, T.N., Garibov, A.A., Melikova, S.Z., Jabarov, S.H. & Akhundzada, H.V. (2021). Radiation-thermocatalytic and thermocatalytic properties of n-ZrO_2-n-SiO_2 systems in the process of obtaining hydrogen from water at different temperatures. Journal of Molecular Structure. 130651.

21) Imanova, G.T. & Kaya, M. (2021). Importance of the Radiations in Radiolysis Processes for Hydrogen Generation. Book - Generis publishing. ISBN: 978-1-63902-693-7. 50.

22) Imran, A., Imanova, G.T., Mbianda, X.Y., & Alharbi, M.L.O. (2022). Role of the radiations in water splitting for hydrogen generation. Sustainable Energy Technologies and Assessments. 101926.

23) Imanova, G. (2022). Molecular hydrogen production by radiolysis of water on the surface of nano-ZrO_2 under the influence of gamma rays. Synthesis and Sintering. 2. 9–13.

24) Imran, A., Tahani Saad, A.G., Alexandr, S., Aleksei, S., Sung‐Hwan, J., Evgeny, G., Fadey, K., Pavel, B., & Imanova, G. T,. (2020). Temperature self-regulating flat electric heaters based on MWCNTs modified polymers, Polymer Bulletin. Springer-Verlag GmbH Germany, part of Springer Nature. 11. 1-15.

25) Akdemir, M., Karakas, D.E., Imanova, G.T., Kivrak, H.D. & Kaya, M. (2021). High Efficiency Biomass-Based Metal-Free Catalyst as a Promising Supercapacitor Electrode for Energy Storage. SSRN Electronic Journal.

26) Hokman, Mahmudov., Telman, Suleymanov., Zumrud, Sabzaliyeva., Gunel, Imanova,, HajiVahid, Akhundzada., Kamala, Azizova., Sabina, Hasanova., & Sadig, Hasanov. (2021). Kinetic Interaction of Hexan Conversion and Oxidation on the Surface of an Al_2O_3 Nanocatalyzer at Room Temperature under the Effect of Gamma Radiation, Hindawi publishing. Journal of Chemistry. 9493765. 6.

27) Agayev, T., Imanova, G. & Imran, A. (2021). IR spectroscopic study of zirconium samples in an H_2O_2 medium, IX International Scientific Conference, Actual problems of solid state physics, (APSSP-2021). November 22-26. Minsk (Belarus). 104.

28) Imanova, G. & Bekpulatov, I. (2021). Investigation on the Electronic Structure of Nanosized Barium Monosilicide Films Produced by Low-energy Implantation of Ba^+ Ions in Si. American Journal of Nano Research and Applications. 9 (4). 32-35.

29) Barkaoui, S. & Imanova, G. (2022). Hydrothermal Synthesis of Co3O4 Urchin-Like and their Catalytic Properties in Co Oxidation. Juniper Online Journal Material Science (JOJMS). 7(1). 555704.

30) Imran, A., & Imanova, G. (2022). Sorbtion: A universal technology for water purification. Advanced Physical Research. 4(1). 5-9.

31) Barkaoui, S., Chakhari, S., Kouass, S., Imanova, G., Dhaouadi, H. & Touati, F. (2022). Influence of Ag-doping-cobalt oxide on the structure, optical properties, morphology and preferential oxidation activity of CO. Advanced Physical Research. 4(1). 22-32.

Turkish Journal of Nuclear Science (2022), Vol. 34, No.1. Page: 33-42. http://dergipark.gov.tr/tjins

TENMAK TURKISH ENERGY, NUCLEAR AND MINERAL RESEARCH AGENCY

TURKISH JOURNAL OF NUCLEAR SCIENCES

Journal homepage https://dergipark.org.tr/en/pub/tjns

Buğra Gökhun BULDUK, Volkan YASAKÇI*, Elif TUTUN, Perihan ÜNAK, Ömer ARAS

Ege University, Institute of Nuclear Sciences, Department of Nuclear Applications, Erzene Mah., No:3, 35100, Bornova/Izmir/TURKEY

* volkan.yasakci@gmail.com

^{44}Ti/^{44}Sc RADYONÜKLİD JENERATÖRÜ İÇİN ^{44}Ti ÜRETİMİNİN İNCELENMESİ

Abstract:

As a positron emitter, Scandium-44 (^{44}Sc) having a short half-life of 3.97 (4) h is a promising PET radionuclide which can be produced ^{44}Ti long-lived parent (60.0 (11) y). In this work, a ^{44}Ti/^{44}Sc generator was designed to produce ^{44}Sc. The separation and purification studies were optimized by using ^{46}Sc (83.787 (16) d) as tracer. Hydroxamate and Dowex resins were used for separation process Sc radioisotopes from titanium. Briefly a ^{44}Ti/^{44}Sc generator system may be a source of ^{44}Sc production in hospitals in future. If it is made suitable for hospital use, a hospital will have the opportunity to work with this generator for many years with a single production.

Özet:

Bir pozitron yayıcı olarak, 3,97 (4) h'lik kısa bir yarı ömre sahip olan scandium-44 (^{44}Sc), uzun ömürlü ^{44}Ti ana çekirdeğinden (60.0 (11) y) üretilebilen umut verici bir PET radyonüklidir. Bu çalışmada ^{44}Sc üretmek için ^{44}Ti/^{44}Sc jeneratör sistemi tasarlanmıştır. Ayırma ve saflaştırma çalışmaları, izleyici olarak ^{46}Sc (83.787 (16) d) kullanılarak optimize edildi. Titanyumdan Sc radioizotopları ayırma işlemi için hidroksamat ve dowex reçineleri kullanılmıştır. Kısaca ^{44}Ti/^{44}Sc jeneratör sistemi gelecekte hastanelerde ^{44}Sc üretim kaynağı olabilir. Hastane kullanımına uygun hale getirilirse bir hastane tek üretim ile bu jeneratör ile uzun yıllar çalışma imkanına sahip olacaktır.

Keywords: ^{44}Sc, ^{44}Ti, ^{44}Ti/^{44}Sc generator, cyclotron, ^{45}Sc(p,2n)^{44}Ti, hydroxamate resin.

Anahtar Kelimeler: ^{44}Sc, ^{44}Ti, ^{44}Ti/^{44}Sc jeneratörü, siklotron, ^{45}Sc(p,2n)^{44}Ti, hidroksamat reçinesi.

1. Introduction

PET radionuclides are produced in cyclotron and as generator products. Recently, the production of PET radionuclides has gained an interest to use in nuclear medicine both in terms of being economical and the ease of the applied method. Currently, the search for other radioisotopes that can replace ^{18}F, the most common PET radionuclide produced in particle accelerators, is still ongoing (Ferreira et al., 2012; Jokerst & Gambhir, 2011). It has been proven that especially the new metallic PET radionuclides have better organ involvement and therefore good solubility (Sadeghi, Enferadi & Nadi, 2011; Walczak et al., 2015). Although ^{44}Sc does not have a single production method, there are also different production conditions. Although this radionuclide is a generator product, it can also be produced in accelerators with different targets (Daraban et al., 2009; Hoehr et al., 2014; Severin et al., 2012). However, the general method is often the method obtained by irradiating the natural scandium compounds of ^{44}Ti. Due to the economic and physical convenience of this method, studies on this subject have increased in recent years (Kerdjoudj et al., 2016a; Lee, Kong & Hur, 2016; V. Radchenko et al., 2016; Valery Radchenko et al., 2017; Wittwer et al., 2011). As a result of loading the main radioisotope into the system and elution with certain chemicals, this process takes seconds. Another feature of the generators is that they can be used for much longer periods than the half-life of the product radionuclide, depending on the half-life of the main radionuclide. Since the half-life of ^{44}Ti, the main radionuclide, is approximately 60 years in this project, the use of a single generator will be possible for many years (Ayranov & Schumann, 2010; Filosofov, Loktionova, & Rösch, 2010; Lange et al.,1999; Pruszyński et al., 2010; Roesch, 2012). This is of great importance in terms of ease of use and economy.

With its long half-life, ^{44}Ti is promising as a ^{44}Ti/^{44}Sc generator. However, the production of ^{44}Ti can be expensive because the irradiation time to reach higher activities is long. There are two primary production methods of ^{44}Ti: the first is ^{45}Sc(p,2n)^{44}Ti reaction in particle accelerators (Daraban et al., 2009; Yug et al., 2005), and the second is using ^{40}Ca with alpha particles (Alliot et al., 2015; Severin et al., 2012; Szkliniarz et al., 2016). For the first method, the optimum parameters for irradiation are 22 MeV proton acceleration for 10 days in a cyclotron. Yet, with these parameters, only about 1 mCi is achieved because of the low cross-section values. After production, a long cooling time is also needed due to the generation of other products. Nevertheless, such other products are negligible because of their short half-lives and are easily separated using resin systems (Valery Radchenko et al., 2017). After the separation of ^{44}Ti using this method, the ^{44}Ti/^{44}Sc generator can be produced using known ways, e.g., as for a ^{99}Mo/^{99m}Tc generator (Filosofov et al., 2010; Kerdjoudj et al., 2016b; Pruszyński et al., 2010; Valery Radchenko et al., 2017; Roesch, 2012). For the second method, when ^{226}Ra is used as an alpha particle on Ca targets, ^{226}Ra can decay with the same energy levels to ^{44}Ti gamma energy levels. Thus, the separation of ^{44}Ti and other products from ^{226}Ra (such as ^{214}Pb) is essential. Of note, ^{44}Ti and ^{214}Pb are not easily separable with gamma spectroscopy.

* Correspondig author: Volkan YASAKÇI, Adres: Ege University, Institute of Nuclear Sciences, Department of Nuclear Applications, Erzene Mah., No:3, 35100, Bornova/Izmir/TURKEY E-mail: volkan.yasakci@gmail.com ORCID: 0000-0002-4133-3886 Bornova, Izmir, 35100. Gönderim: 17/04/2022 Kabul: 28/06/2022.

1. Material and Method

1.1. Reagents and equipment

As for the chemicals used in this study, thin layer chromatography paper (ITLC-silica), $TiCl_4$, $CaCl_2$, methanol, hydrochloric acid, 2,3,5,6-tetrafluorophenol (TFP), oxalic acid, sodium hydroxide (NaOH, pH adjuster), acetonitrile were purchased from Merck Chemical Co. (Darmstadt, Germany); $CaCl_2$, Dowex 1X8, 8-hydroxyquinoline, EDTA (ethylenediaminetetraacetic acid), 2,3,5,6-tetrafluorophenol (TFP), and N-(3-dimethylamino propyl)-N'-ethyl carbodiimide hydrochloride (EDC) were supplied from Sigma Aldrich (Darmstadt, Germany); and Accell resin in the Sep-Pak cartridge was purchased from Waters Co. (Milford, USA).

The following equipment from Ege University Institute of Nuclear Sciences was used: high-performance liquid chromatography (HPLC) SPD-10AV UV/vis and NaI (Tl) scintillation

gamma detector and diode array detector (DAD) (Shimadzu SPD-M20A) systems with LC-10Atvp pump (Shimadzu Corporation, Kyoto, Japan), SIL-20A HT automatic sampler (Shimadzu Corporation, Kyoto, Japan), Inertsil ODS-3 C-18 4.6 × 250 mm HPLC 5 µm column (G.L. Sciences Inc., Tokyo, Japan), column oven (Shimadzu CTO-10ASvp), AR-2000 radio TLC imaging scanner (Eckert & Ziegler, Berlin, Germany), 1024-channel multichannel gamma spectrophotometer with 1 × 1 inch LaBr3(Ce) Detector (ORTEC), and $^{226}RaCl_2$ standard.

1.2. Separation of $^{46}Sc^{+3}$ and Ti^{+4}

The separation of radioactive [^{46}Sc] Sc^{+3} from Ti^{4+} was achieved using either hydroxamate or Dowex resin

1.3. $^{46}Sc^{+3}$ and Ti^{4+} Separation Using Hydroxamate Resin

Hydroxamate resin was prepared by functionalizing the carboxy groups of silica-based weak cation exchanger resin. Initially, Accell resin (0.42 g) was soaked in 8.0 mL of water in a 15 mL falcon tube for approximately one day. 30 µL of 3 M HCl, a fresh solution of TFP (0.8 g) in 250 µL of acetonitrile, and EDC (0.8 mmol) were added. The reaction mixture was mixed for one hour at room temperature using a magnetic stirrer, and then the reaction was continued by mixing for another 3 hours at room temperature. Afterward, the resin was separated by filtration and washed three times with 10 mL of water and then three times with 10 mL of acetonitrile to separate unreacted impurities. The resin containing TFP ester groups was converted into hydroxamate resin by reacting with hydroxylamine in the next step. After 0.01 mol, 694.9 mg of hydroxylamine hydrochloride was dissolved in a mixture of 1 mL of 1.0 M NaOH and 2 mL of methanol. The pH was adjusted to 5.3–5.4 with 25–50 µL of 1.0 M NaOH. Then, the solution was added to the activated resin in a 15 mL falcon tube, and the reaction (pH 5.0–5.2) was continued at room temperature for 18 hours using a magnetic stirrer. The product was purified by filtration and washed five times with 10 mL of water and 10 mL of acetonitrile, then dried in vacuum. 333 mg of dried resin was placed in an empty syringe. Then, the column was activated by washing with 8 mL of acetonitrile, 15 mL of water, and 2 mL of 2.0 M HCl, respectively. The $Ti^{4+}$and $^{46}Sc^{+3}$ mixture was passed through the prepared resin (200 µL) and its radioactivity was counted.

1.4. $^{46}Sc^{+3}$ and Ti^{4+} Separation Using Dowex 1X8 Resin

Here, 10^{-3} M $ScCl_3$ and 10^{-6} M $TiCl_4$ were dissolved in 5 mL of methanol and mixed in equal volumes. Then, $^{46}Sc^{+3}$ was added, and the resulting solution was saturated with 5 mg of 8-hydroxyquinoline. The resin was activated before the prepared solution was passed through Dowex 1X8 resin. For this, a mixture containing 10% NaCl and 0.2% NaOH was heated at 80 °C for 2 hours, passed through the resin, and the resin was activated by passing through 0.5% HCl immediately afterward.

The mixture of $^{46}Sc^{3+}$ and $TiCl_4$ passed through Dowex 1X8 resin was examined with an ORTEC 1024-channel multichannel gamma spectrophotometer with a 1 × 1-inch $LaBr_3$(Ce) detector. At the first, background activity was measured. Then, background and elution spectra were determined. 5 mg of 8-hydroxyquinoline solution and $^{46}Sc^{3+}$ and $TiCl_4$ solutions were mixed and passed through Dowex 1X8 resin. The radioactivity of the eluents was counted on a multichannel analyzer. Then, 200 µL of the elution profiles were obtained by passing through 12 M HCl and their radioactivity counts were determined using a multichannel analyzer. In the last step, the count and gamma spectrum of the 200 µL sample taken from the elution obtained by passing 2 M HCl were determined. In addition, HPLC analyzes of $^{46}Sc^{3+}$ and Ti^{4+} separated by passing through Dowex 1X8 resin were performed.

2. Results and Discussion

Szkliniarz reported that ^{43}Sc, ^{44g}Sc, and ^{44m}Sc were produced by irradiating alpha particles accelerated in the cyclotron, using Ca and natural K targets, and highly pure ^{43}Sc was obtained (Szkliniarz et al., 2016). Cyclotrons are known to be economical and advantageous. Several studies of nuclear reactions with deuterium and protons in cyclotrons have been conducted (Tárkányi et al., 2019). While ^{44}Sc can be produced directly with isotopes of ^{43}Ca and ^{44}Ca, we hypothesized that it is possible to produce a ^{44}Ti/^{44}Sc generator by creating ^{44}Ti by reacting ^{45}Sc with protons or deuterons. The disadvantages of ^{44}Ti that we produced directly under our working conditions compared to cyclotron production are its lower particle energy, lower particle density, and the impurities of ^{226}Ra from other radionuclides in the decay chain. Our results are particularly valuable for individuals or groups that do not have the opportunity to work with a cyclotron within an academic environment. Table 1 presents possible reactions

for ^{44}Ti production expect ^{45}Sc.

Table 1. Q-values and threshold energies to produce 44Ti.

Reaction Products	**Q-value** (keV)	Threshold Energy (keV)
$^{40}Ca(\alpha,\gamma)^{44}Ti$	5.127	0
$^{48}Ti(p,2n+t)^{44}Ti$	-36.747	35.477
$^{48}Ti(d,3n+t)^{44}Ti$	-36.972	38.525
$^{51}V(p,4n+\alpha)^{44}Ti$	-42.076	42.908
$^{48}Ti(n,5n)^{44}Ti$	-43.229	44.139
$^{51}V(d,5n+\alpha)^{44}Ti$	-44.301	46.052
$^{51}V(n,5n+t)^{44}Ti$	-61.890	63.116

In these reactions, the simplest isotope, which can be worked with, is 40Ca. Some of the

by-products that can be formed according to the $^{40}Ca(\alpha,\gamma)^{44}Ti$ reaction are $^{44}Ti(\alpha,p)^{47}V$, $^{44}Ti(\alpha,\gamma)^{48}Cr$, $^{40}Ca(\alpha,p)^{43}Sc$, $^{43}Sc(p,\gamma)^{44}Ti$, $^{44}Ti(p,\gamma)^{45}V$, and $^{45}V(p,\gamma)^{46}Cr$. Based on these results, there was no chemical or radiochemical damage of any by-product. Gamma energies of the ^{226}Ra isotope (used as an alpha source) and of its decay products are presented in Table 2.

Table 2. Gamma energies after 226Ra decay chain (Chisté, Bé, & Dulieu, 2007).

Radioisotope	Gamma Energy (keV)	Half-life
^{226}Ra	81.07	1602 years
	83.78	
	186.1	
	600	
^{210}Pb	47	21 years
^{211}Pb	405	36.1 minutes
	832	
^{212}Pb	239	10.64 hours
^{214}Pb	74.81	26.8 minutes
	77.11	
	295	
	352	
	766	
	785	
^{222}Rn	186	3.8 days
^{214}Po	609	162.3 µseconds
	665	
	768	
	934	
	1120	
	1238	
	1764	
	2118	
^{214}Bi	241	19.9 minutes
	295	
	351	
	785	
^{40}K	1460	10^9 years

Gamma energies for the 44Ti isotope and reaction by-products after 226Ra decay are presented in Table 2.

Table 3. Gamma energies and half-lives of the 44Ti isotope and other primary products after 226Ra alpha particle's reaction with 40Ca.

Radioisotope	Gamma Energy (keV)	Half-life
^{44}Ti	**67.8**	**60 years**
	78.3	
^{46}Sc	889	83.9 days
	1120	
^{52}V	1434	3.76 minutes
^{47}Ca	1308	4.53 days
^{22}Na	511	2.60 years
	1274	
^{24}Na	1369	15 hours
^{38}Cl	1600	37.3 minutes
^{47}V	511	32.6 minutes
^{48}Cr	511	21.6 hours
^{45}V	511	547 mseconds
^{46}Cr	511	0.26 seconds
^{44}Sc	**511**	**3.97 hours**

3.1 Results of Separation with Hydroxamate Resin using ^{46}Sc radiotracer

In this study, we achieved the separation of ^{46}Sc from the target system using hydroxamate and Dowex resins. The results show that hydroxamate resin is suitable for separating ^{46}Sc from the target. With 6 M HCl and hydroxamate resin, 97.4% of the total radioactivity of ^{46}Sc was separated. These results are in line with those reported previously by Gagnon et al., who used hydroxamate resin previously for the separation of ^{45}Sc and who reported that the extraction of ^{45}Ti was possible with > 50% recovery in 1 mL of 1 M oxalic acid (Gagnon et al., 2012). They also reported that this resin could also be used successfully in ^{89}Zr separation. Indeed, in our previous study, the hydroxamate resin was used for the production of ^{89}Zr, whereby 75% of ^{89}Zr was eluted from the hydroxamate resin with oxalic acid (Bulduk et al., 2019).

3.2 HPLC Analysis of the Dowex 1X8 Resin, $ScCl_3$, and $TiCl_4$ Separations

^{46}Sc, a relatively long-lived radionuclide that decays by ß and ɤ radiation with a half-life of 83.8 days of Sc, was used as a carrier to determine Sc separation and purification of ^{46}Sc.

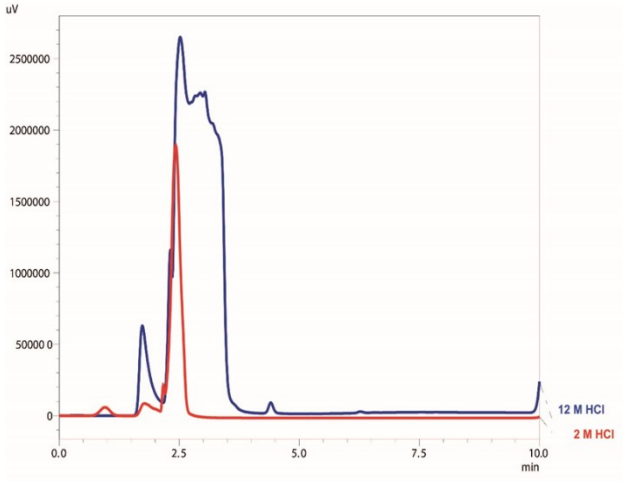

Figure 1. 46Sc elution profile passing through Dowex 1X8 Resin (activity as a percentage).

Figure 1 shows that ^{46}Sc radioactivity can be eluted with 12 M HCl at a rate of 93.86% with Dowex 1X8 resin. Our results agree with Bartos et al. who separated ^{47}Sc with 0.5 M ammonium acetate by adsorbing it on Dowex 50 cation resin. The ^{47}Sc separation efficiency in the proposed procedure is about 90%, with a separation time of fewer than 2 hours. The resulting carrier-free ^{47}Sc was used to label the DOTATATE conjugate (Bartoś et al., 2012).

2. Conclusion

An in-house ^{44}Ti/^{44}Sc generator can be highly valuable for hospitals, making profound contributions to the health system. In addition, such a generator affords the convenience of working with a single generator for many years thanks to the long half-life of ^{44}Ti, dramatically reducing the costs of producing ^{44}Sc.

3. Acknowledgments

This research was supported by the Ege University Research Fund (FGA-2018-20118). B.G. Bulduk was supported by the TUBITAK 2211-C Priority Areas Domestic Doctorate Scholarship Program. Ö. Aras was partially supported by the NIH/NCI Cancer Center Support Grant P30 CA008748.

References

1) Alliot, C., Kerdjoudj, R., Michel, N., Haddad, F. & Huclier-Markai, S. (2015). Cyclotron production of high purity 44m,44Sc with deuterons from 44CaCO3 targets. Nuclear Medicine and Biology, 42(6), 524–529. https://doi.org/10.1016/j.nucmedbio.2015.03.002.

2) Ayranov, M. & Schumann, D. (2010). Preparation of 26Al, 59Ni, 44Ti, 53Mn and 60Fe from a proton irradiated copper beam dump. Journal of Radioanalytical and Nuclear Chemistry, 286(3), 649–654. https://doi.org/10.1007/s10967-010-0732-0.

3) Bartoś, B., Majkowska, A., Krajewski, S. & Bilewicz, A. (2012). New separation method of no-carrier-added 47 Sc

from titanium targets. Radiochimica Acta, 100(7), 457–462. https://doi.org/10.1524/ract.2012.1938.

4) Bulduk, B. G., Ünak, P., Yurt Kılçar, A., Kozguş Güldü, Ö. & Tekin, V. (2019). Analyzing of Production Conditions of 89Zr in the Particle Accelerator. Cumhuriyet Science Journal, 40(2), 388–395. https://doi.org/10.17776/csj.448616.

5) Chisté, V., Bé, M. M. & Dulieu, C. (2007). Evaluation of decay data of radium-226 and its daughters. ND2007. Les Ulis, France: EDP Sciences. https://doi.org/10.1051/ndata:07122.

6) Daraban, L., Adam Rebeles, R., Hermanne, A., Tarkanyi, F. & Takacs, S. (2009). Study of the excitation functions for 43K, 43,44,44mSc and 44Ti by proton irradiation on 45Sc up to 37MeV. Nuclear Instruments and Methods in Physics Research Section B: Beam Interactions with Materials and Atoms, 267(5), 755–759. https://doi.org/10.1016/j.nimb.2009.01.010.

7) Ferreira, C. L., Yapp, D. T. T., Mandel, D., Gill, R. K., Boros, E., Wong, M. Q. & Kiefer, G. E. (2012). 68 Ga Small Peptide Imaging: Comparison of NOTA and PCTA. Bioconjugate Chemistry, 23(11), 2239–2246. https://doi.org/10.1021/bc300348d.

8) Filosofov, D. V., Loktionova, N. S. & Rösch, F. (2010). A 44Ti/44Sc radionuclide generator for potential application of 44Sc-based PET-radiopharmaceuticals. Radiochimica Acta, 98(3). https://doi.org/10.1524/ract.2010.1701.

9) Gagnon, K., Severin, G. W., Barnhart, T. E., Engle, J. W., Valdovinos, H. F. & Nickles, R. J. (2012). 45Ti extraction using hydroxamate resin. AIP Conference Proceedings, 1509(December), 211–214. https://doi.org/10.1063/1.4773970.

10) Hoehr, C., Oehlke, E., Benard, F., Lee, C. J., Hou, X., Badesso, B. & Schaffer, P. (2014). 44gSc production using a water target on a 13MeV cyclotron. Nuclear Medicine and Biology, 41(5), 401–406. https://doi.org/10.1016/j.nucmedbio.2013.12.016.

11) Jokerst, J. V. & Gambhir, S. S. (2011). Molecular Imaging with Theranostic Nanoparticles. Accounts of Chemical Research, 44(10), 1050–1060. https://doi.org/10.1021/ar200106e.

12) Kerdjoudj, R., Pniok, M., Alliot, C., Kubíček, V., Havlíčková, J., Rösch, F. & Huclier-Markai, S. (2016a). Scandium(<scp>iii</scp>) complexes of monophosphorus acid DOTA analogues: a thermodynamic and radiolabelling study with ^{44}Sc from cyclotron and from a ^{44}Ti/^{44}Sc generator. Dalton Transactions, 45(4), 1398–1409. https://doi.org/10.1039/C5DT04084A.

13) Kerdjoudj, R., Pniok, M., Alliot, C., Kubíček, V., Havlíčková, J., Rösch, F. & Huclier-Markai, S. (2016b). Scandium(III) complexes of monophosphorus acid DOTA analogues: A thermodynamic and radiolabelling study with 44Sc from cyclotron and from a 44Ti/44Sc generator. Dalton Transactions, 45(4), 1398–1409. https://doi.org/10.1039/c5dt04084a.

14) Lange, R., D'Auria, J., Giesen, U., Vincent, J. & Ruth, T. (1999). Preparation of a radioactive target. Nuclear Instruments and Methods in Physics Research Section A: Accelerators, Spectrometers, Detectors and Associated Equipment, 423(2–3), 247–255. https://doi.org/10.1016/S0168-9002(98)01289-3.

15) Lee, E.J., Kong, Y.B. & Hur, M. G. (2016). Test production of Ti-44 using RFT-30 cyclotron. Cyclotrons2016, 108–109.

16) Pruszyński, M., Loktionova, N. S., Filosofov, D. V. & Rösch, F. (2010). Post-elution processing of 44Ti/44Sc generator-derived 44Sc for clinical application. Applied Radiation and Isotopes, 68(9), 1636–1641. https://doi.org/10.1016/j.apradiso.2010.04.003.

17) Radchenko, V., Meyer, C. A. L., Engle, J. W., Naranjo, C. M., Unc, G. A., Mastren, T. & Fassbender, M. E. (2016). Separation of 44Ti from proton irradiated scandium by using solid-phase extraction chromatography and design of 44Ti/44Sc generator system. Journal of Chromatography A, 1477, 39–46. https://doi.org/10.1016/j.chroma.2016.11.047.

18) Radchenko, Valery, Engle, J. W., Medvedev, D. G., Maassen, J. M., Naranjo, C. M., Unc, G. A. & Fassbender, M. E. (2017). Proton-induced production and radiochemical isolation of 44Ti from scandium metal targets for 44Ti/44Sc generator development. Nuclear Medicine and Biology, 50, 25–32. https://doi.org/10.1016/j.nucmedbio.2017.03.006.

19) Roesch, F. (2012). Scandium-44: Benefits of a long-lived PET radionuclide available from the 44Ti/44Sc generator system. Current Radiopharmaceuticals, 5(3), 187–201. https://doi.org/10.2174/1874471011205030187.

20) Sadeghi, M., Enferadi, M. & Nadi, H. (2011). 45Ti, a candidate for positron emission tomography: Study of the cyclotron production. Radiochemistry, 53(4), 411–414. https://doi.org/10.1134/S106636221104014X.

21) Severin, G. W., Engle, J. W., Valdovinos, H. F., Barnhart, T. E. & Nickles, R. J. (2012). Cyclotron produced 44gSc from natural calcium. Applied Radiation and Isotopes, 70(8), 1526–1530. https://doi.org/10.1016/j.apradiso.2012.04.030.

22) Szkliniarz, K., Sitarz, M., Walczak, R., Jastrzębski, J., Bilewicz, A., Choiński, J. & Zipper, W. (2016). Production of medical Sc radioisotopes with an alpha particle beam. Applied Radiation and Isotopes, 118, 182–189. https://doi.org/10.1016/j.apradiso.2016.07.001.

23) Walczak, R., Krajewski, S., Szkliniarz, K., Sitarz, M., Abbas, K., Choiński, J. & Bilewicz, A. (2015). Cyclotron production of 43Sc for PET imaging. EJNMMI Physics, 2(1), 33. https://doi.org/10.1186/s40658-015-0136-x.

24) Wittwer, D., Dressler, R., Eichler, R., Gäggeler, H. W., Piguet, D., Serov, A. & Vögele, A. (2011). The thermal release of scandium from titanium metal – a simple way to produce pure 44 Sc for PET application. Radiochimica Acta, 99(3), 193–196. https://doi.org/10.1524/ract.2011.1832.

25) Yug, A., Novgorodov, A. F., Skripnik, A. V., D.V., F., Skripnik, A. V., Kaplun, V. G. & Rösch, F. (2005). 44Ti : Investigation of target preparation, irradiation and yields in the 45 Sc (p, 2n) process. In: Annual Report. Institute of Nuclear Chemistry, University of Mainz (2005), 1993.

Turkish Journal of Nuclear Sciences
Volume: 35 No:1 2022

CONTENTS

Research Articles

Turkish Journal of Nuclear Science (2022), Vol. 35, No.1. Page:1-6. http://dergipark.gov.tr/tjins

TURKISH JOURNAL OF NUCLEAR SCIENCES

Journal homepage https://dergipark.org.tr/tr/pub/tjns

ASSESSMENT OF GEOMETRIC CHANGES IN REGION OF INTEREST AND ITS DOSIMETRIC CONSEQUENCES USING DEFORMABLE IMAGE REGISTRATION FOR HEAD AND NECK ADAPTIVE RADIATION THERAPY

Sümeyra CAN[1], Didem KARAÇETİN[2]

[1-2]Istanbul Basaksehir Cam and Sakura City Hospital

*sumeyracn@gmail.com,

BAŞ VE BOYUN ADAPTİF RADYOTERAPİ İÇİN DEFORMABLE GÖRÜNTÜ KAYDI KULLANILARAK İLGİLİ BÖLGEDEKİ GEOMETRİK DEĞİŞİMLERİN VE DOZİMETRİK SONUÇLARIN DEĞERLENDİRİLMESİ

A :

The aim of this study was to evaluate the change in volume and center of mass for a region of interest (ROI) and how changes affect the cumulative dose through Geometric Processing Unit (GPU)-based Deformable Image Registration.

Ten head and neck cancer patients treated with simultaneous integrated boost in tomotherapy were analyzed retrospectively. Planning computed tomography (CT) and pretreatment weekly CT images were obtained for each patient. Cumulative dose and geometric changes were calculated for critical organs using these images, GPU-based image recording. The cumulative dose was evaluated according to geometric changes and compared with the planned dose.

There was no statistical difference between the cumulative dose and the planned dose for D_{mean}, V100% and V90% of planning target volume (PTV1) ($p > 0.05$). However, the cumulative dose was 14.8% and 8.8% lower than the planned dose for V100% and V95% of PTV3, respectively. The cumulative dose delivered to the spinal cord was 7% higher than the planned dose; however, 6.6% and 4.1% were less than the planned dose for the left and right parotid glands, respectively.

Because head and neck cancer patients undergo many anatomical changes during treatment, cumulative dose assessment is an important parameter for determining how well treatment planning is actually being achieved. GPU-based three dimensional (3D) deformable image registration enables real-time assessment of dose accumulation and tracking of inter-fraction volume variation for a region of interest. Deformable image recording is an important tool for the evaluation of adaptive radiotherapy.

Key Words : Adaptive Radiotherapy, Deformable Image Registration, Head and Neck Cancers, Radiation Dose, Tomotherapy

:

Bu çalışmanın amacı, ilgilenilen bir bölge için hacim ve kütle merkezindeki değişimi ve değişikliklerin kümülatif dozu nasıl etkilediğini Geometrik İşlem Birimi (GPU) tabanlı deforme edilebilir görüntü kaydı yoluyla değerlendirmekti. Tomoterapide simültane entegre boost ile tedavi edilen on baş boyun kanseri hastası retrospektif olarak analiz edildi. Her hasta için planlama BT ve tedavi öncesi elde edilen haftalık BT görüntüleri elde edildi. Bu görüntüler, GPU tabanlı görüntü kaydı kullanılarak kritik organlar için kümülatif doz ve geometrik değişiklikler hesaplandı. Kümülatif doz geometrik değişikliklere göre değerlendirildi ve planlanan doz ile karşılaştırıldı.

Plananlanan hedef hacmin (PTV_1) D_{mean}, V_{100} ve V_{90}'ı için kümülatif doz ile planlanan doz arasında istatistiksel bir fark yoktu ($p > 0.05$). Ancak kümülatif doz, PTV_3'ün V_{100} ve V_{95}'i için sırasıyla planlanan dozdan sırasıyla %14,8 ve %8,8 oranında daha düşük olduğu görüldü. Medulla spinalise verilen kümülatif doz, planlanan dozdan %7 daha yüksekti; ancak sol ve sağ parotis bezleri için sırasıyla planlanan dozdan sırasıyla %6,6 ve %4,1 daha azdı.

Baş boyun kanseri hastaları tedavi boyunca birçok anatomik değişiklik geçirdiğinden kümülatif doz değerlendirmesi tedavi planlamasının ne kadar gerçekte sağlandığını belirlemek için önemli bir parametredir. GPU tabanlı 3 boyutlu (3D) deforme edilebilir görüntü kaydı, gerçek zamanlı doz birikiminin değerlendirilmesini ve ilgilenilen bir bölge için fraksiyonlar arası hacim değişiminin takip edilmesini sağlar. Deforme edilebilir görüntü kaydı, adaptif radyoterapinin değerlendirilmesi için önemli bir araçtır.

Anahtar Kelimeler: Adaptif radyoterapi, Baş boyun kanserleri, Deforme edilebilir görüntü kaydı, Radyasyon dozu, Tomoterapi

***Corresponding author: Sumeyra CAN, PhD, [1-2]Istanbul Basaksehir Cam and Sakura City Hospital Istanbul Basaksehir Cam and Sakura City Hospital, Başakşehir Mah. G-434 Cad. No: 2L Başakşehir / İSTANBULTÜRKİYE, mail: sumeyracn@gmail.com, Phone: +90 (553) 686 7040 ORCID:0000-0003-1991-9774 .

1. Introduction

Radiotherapy, along with surgery and/or chemotherapy, is the main treatment for head and neck cancers (Atwell, 2020). Modern therapy techniques, namely intensity modulated radiation therapy and volumetric arc radiation therapy, allow the delivery of the treatment dose to target volumes while simultaneously sparing critical structures. On the other hand, patients with head and neck cancer undergo many anatomical changes caused by weight loss during radiotherapy (Toledano, 2012). In addition, tumor volume and parotid gland volume decrease, and this decrease is usually asymmetrical (O'Daniel, 2007; Sharma, 2020;). Innovations in patient immobilization and imaging technology allow us to minimize setup uncertainties; however, there may be differences between planned and absorbed doses due to anatomical changes. Anatomical change can be evaluated using kilo- voltage computed tomography (kVCT) or mega voltage computed tomography (MVCT) scans with an advanced imaging system (Heukelom, 2020; Lowther, 2020; Kanehira, 2020).

Adaptive radiation therapy (ART) is to revise the original treatment plan based on the patient's random or systematic anatomical changes during 6-7 weeks of fractionated radiotherapy, thereby improving the quality of treatment (Capelle, 2012). In ART, the patient's CT image is taken again and after the new contouring and re-planning, the patient continues the treatment according to the new treatment plan. However, manual target critical structures delineation in offline ART takes time (Loo, 2011; Veiga, 2014). Recent studies have shown that deformable image registration (DIR) plays a crucial role in ART to monitor anatomical changes (Fung, 2020). In addition, it is possible to determine target volumes and calculate the cumulatively absorbed dose in the respective volumes via DIR, however, image quality is very important (Veiga, 2015; Zhang, 2018; Scaggion, 2020). Although MVCT scans can confirm the patient's position and anatomical change, they have lower quality than kVCT scans for soft tissues (Nobnop, 2019).

On the same ground, in this study, it was aimed to evaluate changes in volume and center of mass and how these changes affect the cumulative dose for the region of interest, considering patient-specific anatomy with Geometric Processing Unit (GPU)-based Deformable Image Registration.

2. Materials and Methods

2.1. Patient population and Target delineation

Ten head and neck cancer patients treated with Tomotherapy Hi-Art (Accuray Inc., Sunnyvale, CA, USA) using the simultaneous integrated boost (SIB) technique were selected for this study. Seven patients were diagnosed with tonsil malignant neoplasm, 1 patient with nasopharyngeal CA, and 2 patients with tonsil carcinoma. Weight changes in patients were recorded before and after treatment. Patient information is shown in Table 1.

Table 1. Patients' characteristic regarding treatment

Patient ID	Diagnosis	Prescription Dose (Gy)	Tx Duration (Day)	Weight Change (kg)
1	Tonsil CA	70.00	53	8.80
2	Base of Tongue	70.00	51	2.00
3	Nasopharynx	69.96	47	5.40
4	Tonsil CA	70.00	56	10.90
5	Tonsil CA	70.00	39	7.00
6	Tonsil CA	70.00	50	2.10
7	Tonsil CA	70.00	43	9.60
8	Tonsil CA	70.00	45	11.50
9	Tonsil CA	70.00	43	4.40
10	Base of Tongue	70.20	50	10.70

For treatment planning, a planning CT image with a slice thickness of 3 mm was taken for each patient. Three different target volumes were defined for each patient. Thermoplastic masks with head and neck micro-perforations were used for patient immobilization. All targets, including clinical target volume (CTV_1) (gross volume of disease), CTV_2 (next stage nodal regions), and CTV_3 (areas harboring subclinical disease) were contoured in relation to other anatomical boundaries of the structures. Tighter margins have been added to create planning target volumes (PTVs). Based on our clinical protocol, PTVs were generated from respective CTVs by adding a 3mm margin with all expansions for setup uncertainties. In addition to the parotid glands, brain stem, medulla spinalis, mandible, and oral cavity, optic nerves, lenses, and eyes were contoured for dosimetric analysis.

2.1. Treatment Planning and Evaluation

Helical tomotherapy plans were created with Accuray's integrated treatment planning system (TPS) Hi-Art PlanningStation 5.1.1.6 using the TomoTherapy (Accuray Inc., Sunnyvale, CA, USA) platform. The prescription dose of PTV_1 was 70 Gy in 35 fractions with a minimum coverage of 95% for all treatment plans while protecting as much critical structures as possible. In addition, 62.7 and 56.1 Gy were prescribed for PTV_2 and PTV_3, respectively. The field width was defined as 2.5 cm, the eigen factor was 0.277, and the modulation factor was 2.5. Dose restrictions for helical tomotherapy plans were optimized according to the Radiation Therapy Oncology Group (RTOG) 0615 protocol. Data from dose volume histograms (DVHs) of all plans were used to determine the dosimetric difference between the planned dose and the cumulative dose. $V_{100\%}$, $V_{95\%}$, $V_{90\%}$ (volume that receives 100%, 95%, 90% of prescription dose) and D_{mean} (mean dose) of target volumes were considered to evaluate tumor coverage. In addition, the maximum dose (D_{max}) for the spinal cord and brain stems was limited to <45 Gy and <54 Gy, respectively. Also, D_{mean} for the parotid glands was limited to <26 Gy. Also, D_{max} for lenses, optic nerves, eyes was taken into account.

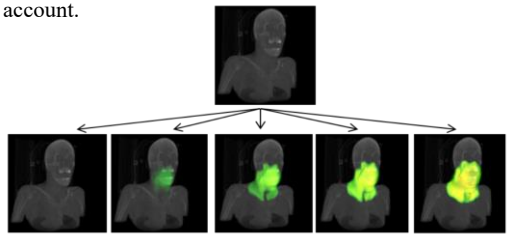

Figure 1. Tumor coverage and weekly delivered dose through DIR during 6 weeks of the treatment course for selected case. (Patient-3)

2.2. The change in volume and center of mass for ROI

Six to eight Daily kVCTs obtained to correct set-up errors before the treatment were selected for each patient in this study. In order to perform kV-to-kV registration, alignment was done to provide a close overlaid for two scans as much as possible, so, these kVCTs were superimposed on the planned CT images to delineate targets and critical structures. And then resizing and resampling of CT images were performed to track anatomical changes via GPU based deformable image registration algorithm. Deformation vector fields obtained based on each Cartesian direction were used for contour propagation to map the delineated ROI on planning CT to each weekly kVCT. A Jacobian analysis was performed for the deformed anatomy. In order to determine non-rigid change in the patient setup, deformation based on each contoured structure was evaluated. U, V, and W matrices were used for the Jacobian determinant for each voxel to evaluate the volumetric changes in the target volumes and surrounding critical structures. The determinant was defined as follows:

$$J_i = \begin{vmatrix} \frac{dU}{dx_i} & \frac{dU}{dy_i} & \frac{dU}{dz_i} \\ \frac{dV}{dx_i} & \frac{dV}{dy_i} & \frac{dV}{dz_i} \\ \frac{dW}{dx_i} & \frac{dW}{dy_i} & \frac{dW}{dz_i} \end{vmatrix} \quad (1)$$

The change in the center of mass and the distance between the PTVs and the left and right parotid glands were determined based on Cartesian coordinates using DIR helped to compensate for the inter-fractional motion of the target volumes and critical organs. The doses were then recalculated from each kVCT to determine the actual delivered dose to the targets and the critical structures. Linear interpolation was used for the dose mapping. The cumulative dose was calculated by summing, week by week, to obtain the total absorbed dose. In order to make a comparison between the accumulated dose and the planned dose, Gamma analysis was performed. Based on our model, all patients were treated identically, and the change in anatomy was not considered for dose distribution. For Gamma analysis, 1% and 1 mm were chosen as the default criteria. Gamma analysis was defined by:

$$\Gamma(\vec{r_e}, \vec{r_r}) = \sqrt{\frac{r^2(\vec{r_e}, \vec{r_r})}{\Delta d^2} + \frac{\delta^2(\vec{r_e}, \vec{r_r})}{\Delta D^2}} \quad (2)$$

where Δd and ΔD are the distance to agreement and HU difference criteria, respectively, r_e is the position at the evaluated pixel, and r_r is the position of the reference voxel (Guerrero, 2006).

2.3. Statistical analysis

Finally, SPSS statistical software version 28.0.1. (SPSS, Chicago, IL, USA) was used to examine the statistical differences in each of the planned dose obtained from helical tomotherapy plans and the delivered dose obtained by a GPU-based 3D image deformation/visualization tool. A paired sampled t-test was applied to determine the difference between planned and accumulated doses. For this study, according to the null hypothesis, there should be no difference between the mean planned dose and the mean cumulative dose. In addition, correlation analysis was applied to evaluate the effect of geometric changes in volume and center of mass (COM) displacement on the delivered dose to both parotid glands. Based on Pearson's correlation, it was measured whether there is a linear dependence between the aforementioned variables. Pearson's correlation was defined by:

$$r = \frac{\Sigma(x - m_x)(y - m_y)}{\sqrt{\Sigma(x - m_x)^2}\sqrt{\Sigma(y - m_y)^2}} \quad (3)$$

where mx and my were the mean of geometric changes in volume and COM displacement, respectively. The p value (significance level) of the correlation was calculated based on the t value, which is defined by:

$$t = \frac{r}{\sqrt{1 - r^2}}\sqrt{n - 2} \quad (4)$$

Statistical significance of $p < 0.05$ was considered for both analyses. If the p value was < 5%, the correlation was considered statistically significant.

3. Results

3.1. Cumulative dose for PTVs

Based on the Jacobian and Gamma analysis, the accumulated dose versus planned dose was evaluated for ROI. Planned and accumulated doses for target volumes were listed in Table 2 and Table 3, respectively. According to the test results, there was no statistical difference between the accumulated dose and the planned dose for D_{mean}, $V_{100\%}$ and $V_{90\%}$ of PTV_1 ($p>0.05$); however, there was a statistical difference between the planned dose and the accumulated dose for V_{95} of PTV_1 with a maximum difference of 8.6%. The accumulated dose was ~3% lower than the planned dose for $V_{95\%}$ of PTV_1; however, the planned dose was delivered to PTV_1 as expected considering D_{mean}, $V_{100\%}$ and $V_{90\%}$. Tumor coverage and weekly delivered dose for the selective case was shown in Figure 1. Additionally, there was no statistical difference between the accumulated dose and the planned dose for PTV_2 ($p>0.05$); however, dose differences were observed in $V_{100\%}$ and $V_{95\%}$ of PTV_3 ($p<0.05$). The accumulated dose was 14.8% and 8.88% lower than the planned dose for $V_{100\%}$ and $V_{95\%}$ of PTV_3, respectively. The dosimetric comparison between planned and accumulated doses for target volumes was shown in Figure 2. All p-values and plan evaluations for the ROI were listed in Table 5. Moreover, weekly doses were shown in Figure 3 for target volumes from ten patients. As a result, the planned dose was delivered to the target volumes; however, dose discrepancies were observed for several parameters of PTVs in the patient where maximum weight loss was observed.

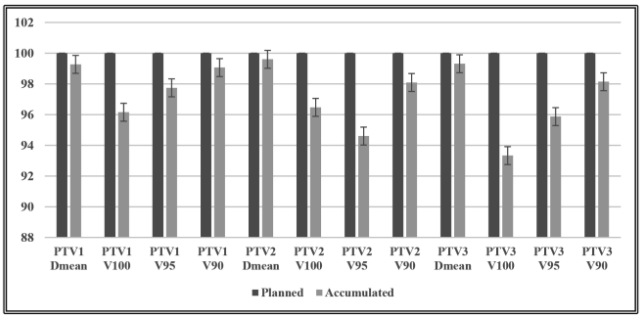

Figure 2. Dosimetric comparison between planned and accumulated dose for target volumes. All parameters are normalized to 100%

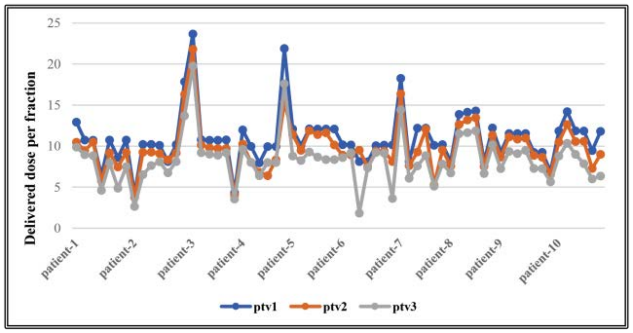

Figure 3. Weekly delivered dose were shown for target volumes from ten patients. $D_{95\%}$ of target volumes were considered.

Table 2: Planned dose of target volumes.

	Planned Dose											
	PTV1				PTV2				PTV3			
Patient ID	D_{mean} Gy	V100 (70 Gy) %	V95 (66.5 Gy) %	V90 (63 Gy) %	D_{mean} Gy	V100 (63 Gy) %	V95 (59.8 Gy) %	V90 (56.7 Gy) %	D_{mean} Gy	V100 (57 Gy) %	V95 (54.1 Gy) %	V90 (51.3 Gy) %
1	70.97	91.40	99.85	100.00	71.21	94.03	100.00	100.00	70.46	78.62	92.46	96.54
2	70.75	87.63	97.66	99.77	70.80	86.88	99.90	100.00	66.90	94.09	99.34	95.32
3	71.00	86.57	96.59	98.35	64.54	99.53	99.79	99.92	66.87	89.87	98.62	97.94
4	71.72	91.17	99.70	99.97	68.93	91.17	99.70	93.57	57.56	94.94	99.94	100.00
5	70.94	90.03	98.93	99.69	68.74	90.03	98.93	98.01	57.40	99.91	99.97	100.00
6	70.96	92.31	99.44	99.79	67.52	96.89	92.31	90.88	64.47	94.29	94.32	96.89
7	71.10	88.28	99.42	99.99	70.66	94.29	98.14	99.98	66.91	88.28	94.17	99.56
8	70.81	80.01	95.18	98.75	67.23	96.13	99.40	96.60	58.25	91.99	98.00	99.62
9	67.01	86.57	98.23	99.39	65.56	91.99	98.98	90.60	58.48	92.22	96.28	99.23
10	71.01	91.34	99.82	100.00	66.11	93.28	99.56	99.91	61.93	93.42	94.09	99.24
Mean	70.14	88.53	98.48	99.57	68.13	93.42	98.67	96.94	62.92	91.76	96.71	98.43

Table 3: Accumulated dose of target volumes

	Accumulated Dose											
	PTV1				PTV2				PTV3			
Patient ID	Dmean Gy	V100 (70 Gy) %	V95 (66.5 Gy) %	V90 (63 Gy) %	D_{mean} Gy	V100 (63 Gy) %	V95 (59.8 Gy) %	V90 (56.7 Gy) %	D_{mean} Gy	V100 (57 Gy) %	V95 (54.1 Gy) %	V90 (51.3 Gy) %
1	70.83	87.44	99.33	99.96	71.03	91.55	99.24	99.93	70.52	73.81	94.38	98.19
2	70.50	90.37	98.03	99.40	70.98	93.20	99.85	100.00	67.28	90.37	91.40	94.40
3	70.95	83.29	96.69	99.45	64.76	95.76	96.59	98.35	65.93	87.09	91.55	97.66
4	71.63	90.77	98.11	99.35	69.51	91.28	83.29	94.80	57.90	86.57	96.95	98.35
5	70.92	89.81	98.82	99.58	69.09	83.11	91.17	98.54	57.53	89.78	94.94	99.70
6	70.95	90.88	98.39	99.38	67.43	86.08	86.86	92.31	64.33	88.50	89.53	90.85
7	71.03	86.03	98.41	99.87	70.53	87.66	93.40	98.05	67.19	87.99	90.03	92.67
8	68.16	87.63	91.55	96.13	65.83	87.54	91.10	95.18	56.89	82.89	96.78	99.73
9	66.18	75.92	90.38	95.04	64.48	92.37	95.44	83.25	58.02	88.21	95.32	96.84
10	70.00	69.11	92,92	98.22	64.98	92.75	96.57	90.60	59.31	81.30	86.41	97.65
Mean	70.11	85.12	96.26	98.63	67.86	90.13	93.35	95.10	62.49	85.65	92.72	96.60

3.2. Cumulative dose for OARs

A paired sample t-test was also applied for the medulla spinalis and parotid glands. Overdose of the medulla spinalis was observed in two patients, and the accumulated dose was higher than the planned dose by 18.4% and 26.2% in Patient-7 and Patient-10, respectively. On the other hand, there was no statistical difference between the accumulated dose and planned dose considering all patient data for the medulla spinalis ($p = 0.211$). Additionally, there was a statistical difference between the planned dose and accumulated dose for the left parotid gland ($p = 0.045$), and the delivered dose was less than the planned dose by 6.6%. On the other hand, there was no statistical difference between the planned dose and accumulated dose for the right parotid gland ($p = 0.07$). Moreover, the accumulated dose was lower than the planned dose by ~ 4% for the right parotid gland. The weekly delivered doses of the left and right parotid glands from each patient were shown in Figure 4 and Figure 5. As a result, the planned dose was delivered to the organs at risk (OARs). The difference between the planned dose and the accumulated dose for critical structures was given in Table 4.

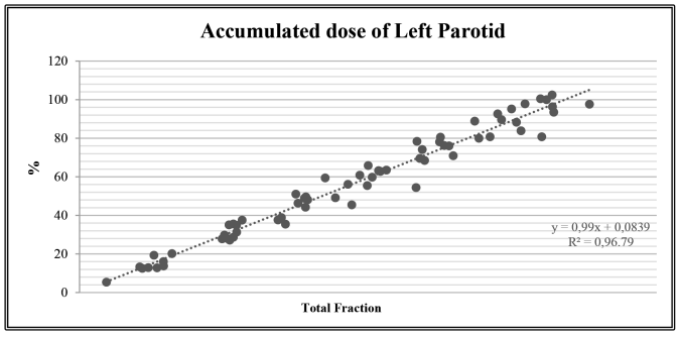

Figure 4. % Ratio of accumulated dose to planned for left parotid glands from all patients.

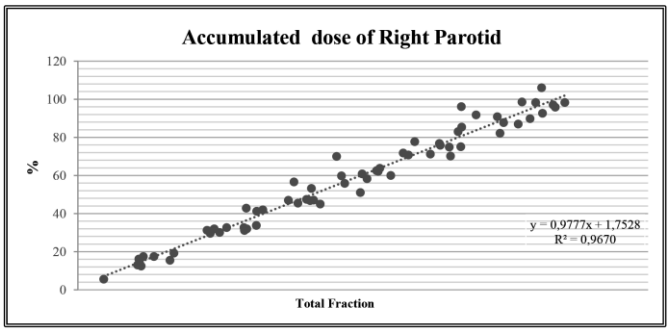

Figure 5. % Ratio of accumulated dose to planned for left parotid glands from all patients.

Table 4: Planned and accumulated dose for critical structures.

	Medulla Spinalis D_{max} (Gy)		Left Parotid Gland D_{mean} (Gy)		Right Parotid Gland D_{mean} (Gy)	
Patient ID	Planned	Accumulated	Planned	Accumulated	Planned	Accumulated
1	43.30	41.81	22.60	21.12	34.52	34.04
2	41.90	43.67	23.98	23.10	56.75	55.80
3	33.22	30.69	56.44	56.70	49.08	47.05
4	40.74	40.96	37.33	30.13	23.65	22.73
5	39.65	39.14	36.46	32.19	24.76	22.49
6	39.72	43.67	25.25	24.69	24.87	23.04
7	43.07	51.00	40.95	39.96	14.12	14.97
8	41.44	41.77	27.63	28.31	23.13	22.73
9	43.10	41.55	7.58	7.58	38.95	37.82
10	42.39	57.51	22.90	18.50	20.97	17.90
Mean	40.85	43.17	30.11	28.22	31.08	29.85

Table 5: Plan comparison for target volumes and organs at risk

	p Values	
PTV1 D_{mean}	0.083	> 0.05
PTV1 V_{100}	0.216	> 0.05
PTV1 V_{95}	0.041	< 0.05
PTV1 V_{90}	0.093	> 0.05
PTV2 D_{mean}	0.250	> 0.05
PTV2 V_{100}	0.072	> 0.05
PTV2 V_{95}	0.060	> 0.05
PTV2 V_{90}	0.142	> 0.05
PTV3 D_{mean}	0.188	> 0.05
PTV3 V_{100}	0.010	< 0.05
PTV3 V_{95}	0.004	< 0.05
PTV3 V_{90}	0.060	> 0.05
Medulla Spinalis D_{max}	0.211	> 0.05
Left Parotid Gland D_{mean}	0.045	< 0.05
Right Parotid Gland D_{mean}	0.070	> 0.05

*p = Significance

3.3. The Change in volume and COM displacement

Since head and neck cancer has a complex shape and many factors can affect tumor location and size, weight loss did not affect the volume shrinkage of targets by itself. The mean volume reduction in

PTV_1 was 3.3 % (range of 6.3%–1%), PTV_2 was approximately 7% (range of 18 – 0.8%), CTV_3 volume was 8.6% (range of 18 – 5.2%). The mean volume reduction in the right parotid gland was 11.7 % (range of 29.3 - 1.3 %). The mean volume reduction in the left parotid gland was 13.5 % (range of 25.9 - 5.7 %). The weekly volume change of the ROI was shown in Figure 6. The mean reduction in the distance between the parotid glands was 2.2 % (range of 3- 0.5 %). The average change in distance between the center of mass of the ROI and the parotid glands of ten patients during the treatment course was shown in Table 6. Even though the decrease in the distance was small, it caused a change in the dose delivered to the parotid glands.

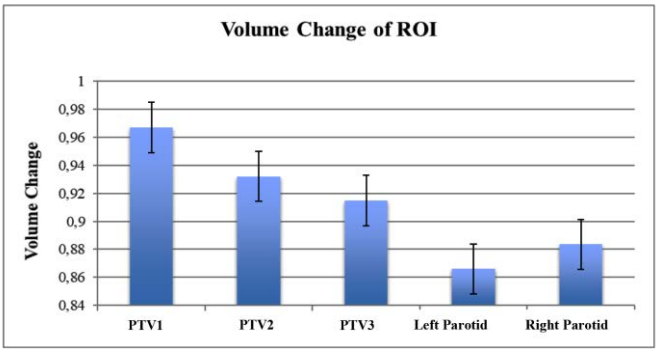

Figure 6. Volumetric Changes of ROI from 10 patients during the treatment course. The volumes were normalized to the planning volume. Average volume change was considered. Error bars are standard error.

Table 6. Average change in distance between center of mass of ROI and parotid glands of ten patients during the treatment course.

	Average Change in Distance		
Patient ID	Right Parotid – PTV1 (mm)	Left Parotid – PTV1 (mm)	Right Parotid – Left Parotid (mm)
1	6.41	6.27	11.12
2	7.56	5.15	10.58
3	6.72	6.93	12.64
4	4.74	9.06	12.55
5	4.36	8.29	11.70
6	8.01	5.97	11.89
7	5.18	7.31	20.01
8	5.37	7.46	12.04
9	8.46	4.41	11.19
10	7.45	6.75	12.00
Mean	6.42	6.76	12.57

Moreover, correlation analysis was applied to each patient to evaluate the effect of the change in volume and COM of critical structures and target volume on composite dose, was shown in Table 7. A strong negative correlation was obtained between volume change and composite dose of the left and right parotid glands (r=-0.25 and r = -0.90). The same analysis was also applied to determine the correlation between the COM displacement of the PTV - right parotid, PTV - left parotid, and both parotid glands. A strong positive correlation was obtained for the right parotid gland (r=0.449); however, this correlation was not statistically significant (p=0.193). Additionally, a strong positive correlation was also obtained for the left parotid (r=0.826) and this correlation was not statistically significant (p=0.03). Since the tumor location was closer to the left parotid gland and the shift was observed towards the left side, the COM displacement increased the composite dose of the left parotid gland.

Table 7. Correlation between the distance of parotid glands to PTV and accumulated dose.

	Correlation between Distance and Accumulated Dose	
	r values	p values
Right Parotid Gland	0.499 (> 0.05)	0.193 (> 0.05)
Left Parotid Gland	0.826 (> 0.05)	0.03 (< 0.05)

*r = Correlation Coefficient

*p = Significance

4. Discussion

Effective radiotherapy requires knowledge of the accumulated dose of ROI and the evaluation of the treatment results during the entire treatment course. Structural delineation and quantification of the change in volume of ROI between the planning CT and daily kVCT and/or MVCT images is possible with DIR (Weppler, 2020). The obtained results based on in-room daily kVCT data showed that DIR is an essential tool for tracking the volume of the ROI and the distance between the target volume and critical structures because the image resolution of kV CT is superior to MVCT (Zhang, 2018). For this reason, many studies focused on the dose evaluation of OARs kV-kV alignment via DIR (Pukala, 2016; Branchini, 2017).

McIntosh et al. used an atlas-based approach to predict the dose. The predicted dose distribution was converted to a complete treatment plan via voxel-based dose-mimicking optimization. Target volume coverage and the dose of critical organs were evaluated. Based on their result, for target coverage, automated plans achieved of 0.6% overdose and 2.4% lower dose for OARs. Additionally, a GPU based-3D image framework was used to evaluate real-time dose accumulation and to track inter-fractional anatomical change for ROI. Moreover, the optical flow registration was used for the kV to kV alignment (McIntosh, 2017).

Elstrom et al. evaluated daily kV cone beam CT and deformable image registration for one patient. Fractional dose and change in volume of the parotid glands and PTVs were taken into account. The volume change between the planning and final fraction was 30% (Elstrøm, 2010).

On the other hand, volume change and change in the center of mass for the parotid glands and target volumes were investigated in this study. Even though the DIR is an essential tool to track anatomical changes, there are still unknown questions regarding these changes that fluctuate among patients. In addition, weekly cumulative dose assessment plays a crucial role in quantifying whether the planned dose is delivered to the target while protecting organs at risk. DIR has been a vital method for radiation therapy applications; however, its integration into clinical practice requires further investigation. Moreover, dose accumulation via DIR is still under development and DIR cannot be used directly in clinical practice due to the limitations of dosimetric and clinical studies. On the other hand, DIR is a crucial step for adaptive radiation therapy ART; because modification of the treatment plan based on maintaining treatment objectives is aimed for ART.

5. Conclusion

One of the main problems in head and neck radiation therapy is the location of a tumor that is in close proximity to the surrounding structures. In addition, patients undergo many anatomical changes during the course of a radiation treatment. It was showed that, the in-house developed GPU based-3D image framework is an essential tool to allow for evaluation real time dose accumulation and tracking inter fractional volume change of ROI for adaptive radiation therapy. Additionally, the efficacy of radiation treatment depends on tracking geometric changes and their dosimetric consequences followed GPU-based algorithm systematically.

Acknowledgments

The authors are indebted to the University of California Los Angeles (UCLA) Radiation Oncology Department for their support providing head and neck cancer patients' data treated with tomotherapy. Theoretical calculations based on GPU-based deformable image registration algorithm and data analysis would have been impossible without the kind collaboration of Daniel Low, Professor, and Vice Chair of Medical Physics at UCLA, Sharon Qui, Anand Santhanam, and John Neylon.

Ethical Approval

For this type of study formal consent is not required in our Institution or The IRB was obtained without patient's information consent.

Informed Consent

Informed consent was obtained from all individual participants included in the study.

References

1) Atwell, D., Elks, J., Cahill, K., Hearn, N., Vignarajah, D., Lagopoulos, J., & Min, M. (2020). A review of modern radiation therapy dose escalation in locally advanced head and neck cancer. *Clinical Oncology*, *32*(5), 330-341.

2) Toledano, I., Graff, P., Serre, A., Boisselier, P., Bensadoun, R. J., Ortholan, C., ... & Lapeyre, M. (2012). Intensity-modulated radiotherapy in head and neck cancer: results of the prospective study GORTEC 2004–03. *Radiotherapy and Oncology*, *103*(1), 57-62.

3) O'Daniel, J. C., Garden, A. S., Schwartz, D. L., Wang, H., Ang, K. K., Ahamad, A., ... & Dong, L. (2007). Parotid gland dose in intensity-modulated radiotherapy for head and neck cancer: is what you plan what you get?. *International Journal of Radiation Oncology* Biology* Physics*, *69*(4), 1290-1296.

4) Sharma, A., & Bahl, A. (2020). Intensity-modulated radiation therapy in head-and-neck carcinomas: Potential beyond sparing the parotid glands. *Journal of Cancer Research and Therapeutics*, *16*(3), 425.

5) Heukelom, J., Kantor, M. E., Mohamed, A. S., Elhalawani, H., Kocak-Uzel, E., Lin, T., ... & Sonke, J. J. (2020). Differences between planned and delivered dose for head and neck cancer, and their consequences for normal tissue complication probability and treatment adaptation. *Radiotherapy and Oncology*, *142*, 100-106.

6) Lowther, N. J., Marsh, S. H., & Louwe, R. J. (2020). Dose accumulation to assess the validity of treatment plans with reduced margins in radiotherapy of head and neck cancer. *Physics and imaging in radiation oncology*, *14*, 53-60.

7) Kanehira, T., Svensson, S., van Kranen, S., & Sonke, J. J. (2020). Accurate estimation of daily delivered radiotherapy dose with an external treatment planning system. *Physics and Imaging in Radiation Oncology*, *14*, 39-42.

8) Capelle, L., Mackenzie, M., Field, C., Parliament, M., Ghosh, S., & Scrimger, R. (2012). Adaptive radiotherapy using helical tomotherapy for head and neck cancer in definitive and postoperative settings: initial results. *Clinical Oncology*, *24*(3), 208-215.

9) Loo, H., Fairfoul, J., Chakrabarti, A., Dean, J. C., Benson, R. J., Jefferies, S. J., & Burnet, N. G. (2011). Tumour shrinkage and contour change during radiotherapy increase the dose to organs at risk but not the target volumes for head and neck cancer patients treated on the TomoTherapy HiArt™ system. *Clinical oncology*, *23*(1), 40-47.

10) Veiga, C., McClelland, J., Moinuddin, S., Lourenço, A., Ricketts, K., Annkah, J., ... & Royle, G. (2014). Toward adaptive radiotherapy for head and neck patients: feasibility study on using CT-to-CBCT deformable registration for "dose of the day" calculations. *Medical physics*, *41*(3), 031703.

11) Fung, N. T. C., Hung, W. M., Sze, C. K., Lee, M. C. H., & Ng, W. T. (2020). Automatic segmentation for adaptive planning in nasopharyngeal carcinoma IMRT: time, geometrical, and dosimetric analysis. *Medical Dosimetry*, *45*(1), 60-65.

12) Zhang, L., Wang, Z., Shi, C., Long, T., & Xu, X. G. (2018). The impact of robustness of deformable image registration on contour propagation and dose accumulation for head and neck adaptive radiotherapy. *Journal of Applied Clinical Medical Physics*, *19*(4), 185-194.

13) Scaggion, A., Fiandra, C., Loi, G., Vecchi, C., & Fusella, M. (2020). Free-to-use DIR solutions in radiotherapy: Benchmark against commercial platforms through a contour-propagation study. *Physica Medica*, *74*, 110-117.

14) Nobnop, W., Chitapanarux, I., Wanwilairat, S., Tharavichitkul, E., Lorvidhaya, V., & Sripan, P. (2019). Effect of deformation methods on the accuracy of deformable image registration from kilovoltage CT to tomotherapy megavoltage CT. *Technology in Cancer Research & Treatment*, *18*, 1533033818821186.

15) Guerrero, T., Sanders, K., Castillo, E., Zhang, Y., Bidaut, L., Pan, T., & Komaki, R. (2006). Dynamic ventilation imaging from four-dimensional computed tomography. *Physics in Medicine & Biology*, *51*(4), 777.

16) Weppler, S., Schinkel, C., Kirkby, C., & Smith, W. (2020). Lasso logistic regression to derive workflow-specific algorithm performance requirements as demonstrated for head and neck cancer deformable image registration in adaptive radiation therapy. *Physics in Medicine & Biology*, *65*(19), 195013.

17) Zhang, L., Wang, Z., Shi, C., Long, T., & Xu, X. G. (2018). The impact of robustness of deformable image registration on contour propagation and dose accumulation for head and neck adaptive radiotherapy. *Journal of Applied Clinical Medical Physics*, *19*(4), 185-194.

18) Pukala, J., Johnson, P. B., Shah, A. P., Langen, K. M., Bova, F. J., Staton, R. J., ... & Meeks, S. L. (2016). Benchmarking of five commercial deformable image registration algorithms for head and neck patients. *Journal of applied clinical medical physics*, *17*(3), 25-40.

19) Branchini, M., Fiorino, C., Dell'Oca, I., Belli, M. L., Perna, L., Di Muzio, N., ... & Broggi, S. (2017). Validation of a method for "dose of the day" calculation in head-neck tomotherapy by using planning ct-to-MVCT deformable image registration. *Physica Medica*, *39*, 73-79.

20) McIntosh, C., Welch, M., McNiven, A., Jaffray, D. A., & Purdie, T. G. (2017). Fully automated treatment planning for head and neck radiotherapy using a voxel-based dose prediction and dose mimicking method. *Physics in Medicine & Biology*, *62*(15), 5926.

21) Elstrøm, U. V., Wysocka, B. A., Muren, L. P., Petersen, J. B., & Grau, C. (2010). Daily kV cone-beam CT and deformable image registration as a method for studying dosimetric consequences of anatomic changes in adaptive IMRT of head and neck cancer. *Acta oncologica*, *49*(7), 1101-1108.

TURKISH ENERGY, NUCLEAR AND MINERAL RESEARCH AGENCY
TURKISH JOURNAL OF NUCLEAR SCIENCES
Journal Web Address: https://dergipark.org.tr/en/pub/tjns

TENMAK
TURKISH ENERGY, NUCLEAR AND MINERAL RESEARCH AGENCY

Mustafa Kemal Mahallesi, Dumlupınar Blv. No:192, 06510 Çankaya/Ankara
Phone:+90 312 295 8700 (Santral) - 444 8235
Fax:+90 312 295 87 61 E-mail:journal@tenmak.gov.tr